

**Development of a Ross Filter Based Aluminum Line Radiation (NICKAL2)  
Detector in Madison Symmetric Torus**

By

Nicholas J. Lauersdorf

Senior Thesis

(Physics)

at the

University of Wisconsin-Madison

2018

## Abstract

The Madison Symmetric Torus (MST) has a two-color soft x-ray tomography (SXT) diagnostic that, using the double-filter technique, measures electron temperature ( $T_e$ ) from the slope of the soft x-ray (SXR) continuum. Because MST has an aluminum plasma-facing surface, bright Al line radiation occurs in the SXR spectrum, contaminating measurements of the SXR continuum. In past application of the double-filter technique, these lines have been filtered out using thick Be filters ( $\sim 400\mu\text{m}$  and  $\sim 800\mu\text{m}$ ), restricting the measurement temperature range to  $\geq 1$  keV. Another way to address the line radiation is to explicitly include it into the SXR spectrum analysis. Based on the ROSS filter, a NICKAL2 detector was designed to measure this line radiation and enable the absolute intensities of the aluminum lines to be quantified and incorporated in the SXR spectrum analysis from which  $T_e$  is derived. The NICKAL2 detector will be used to separate and measure  $\text{Al}^{11+}$  and  $\text{Al}^{12+}$  lines, which occur between 1.59 and 2.25 keV. By using multiple detectors with multi-element filters with differing thicknesses, we create passbands in which the dominant emission is the Al line radiation. The edges of the passband occur at the natural absorption edges of the constitutive elements of the filters. Absolute measurement of Al line intensities will enable use of thinner filters in the SXT diagnostic and accurate measurement of  $T_e > 225$  eV. In addition, the NICKAL2 detector can, using the two-color technique, be used to determine  $T_e$  for  $275 \leq T_e \leq 400$  eV.

## Acknowledgments

Though I've only been working at MST for two years, the amazing experience I've had has meant the world to me. Working as an undergraduate research assistant and doing my senior thesis was by far the best part of my college experience. I have learned more about research and the scientific process than I ever could have through my classes alone. Having this opportunity eliminated any doubts I had pertaining to my education and physics when I first started working at MST. I found my love for doing science, and it affirmed my desire to pursue physics and a research-oriented career. Though these benefits were great, nothing could compare to the amazing people that I have come to know and befriend.

Daniel, I feel incredibly indebted to you due to the opportunity of doing a senior thesis in your lab. Without having this experience, I don't think I would have considered going to graduate school, but, now, I am confident that is where my next step leads. It gave me the incredible reassurance and confidence that I needed to know that I have the potential to succeed in graduate school, and it made me realize the joy I find with my field of study.

Lisa, you are a great friend and the best advisor I could have ever hoped for. Whether it was supporting me academically through offering various research opportunities and academic advice or being there for me to talk with every week and destress, it meant a lot and helped me

out immensely in every possible way. I will miss our weekly, random conversations in your office about your epic of a vertical gardening tale, my slapstick comedy of a life, your house updates, and, in general, both our lives. Through the seemingly endless barrage of exams and homework, I always had at least one fun experience to look forward to on a weekly basis. You were a major driving force in helping me realize not only my love for and joy when doing science but also my desire to pursue that in my future studies and career. Any future success I may have in scientific research or elsewhere can, in a large part, be attributed to the incredible guidance, motivation, and support that you have provided me throughout these past three years, and I will always appreciate everything that you've done to help me grow as a scientist and as a person.

And thank you to the rest of the scientists that I have worked closely with. John and Abdul, without your teaching me the engineering knowledge necessary for designing the spectrometer parts and continuously reviewing my sloppy blueprints, this detector would have never been completed. Also, keep fighting for the undergrads, Abdul! Paolo, though your Italian comments in PFM were the bane of my existence when I first started, your model and, once I learned Google Translate was my friend, your comments allowed me to finally understand programming and the amazing things that could be done with it. Also, your long hair is epic, and I grew mine out because of it... Patrick, though I was not in the machine area often, I deeply appreciate your explaining the jungle of diagnostics and wires. I'm still lost walking through there, but at least I can navigate the area without getting electrocuted now.

There is so much more I could say about everyone here, and I cannot thank everyone enough. I have grown so much both academically and, more importantly, as a person due to this experience. As much as I will miss this and wish I could continue working here, I realize that I

must leave and pursue my dreams, hopefully, to graduate school and wherever they may take me after that. It's time for me to hop off the gravy boat, drown for a while, then find a new gravy boat to sail on.

# Contents

<b>Abstract</b>	<b>i</b>
<b>Acknowledgments</b>	<b>ii</b>
<b>1 Introduction</b>	<b>1</b>
1.1 Introduction to the Madison Symmetric Torus . . . . .	2
1.2 X-ray Radiation in MST Plasmas . . . . .	4
1.3 Two-Color Technique . . . . .	8
1.4 Optical Filters and Transmission Curves . . . . .	11
1.5 Motivation for an Al Line Radiation Detector . . . . .	12
1.6 Thesis Overview . . . . .	13
<b>2 NICKAL2 Detector: Detector Design</b>	<b>15</b>
2.1 Inner Housing Design . . . . .	16
2.2 Housing Geometry . . . . .	23
<b>3 NICKAL2 Detector: Filter Design</b>	<b>27</b>
3.1 Ross Filter. . . . .	28
3.2 General Design . . . . .	31
3.3 Optimization Process . . . . .	35
3.4 Theoretically Optimal Design . . . . .	37
3.5 Final Design . . . . .	39
<b>4 Simulated Signal Analysis</b>	<b>44</b>

4.1	Al Line Radiation Dependence on $n_e$ . . . . .	46
4.2	Al Line Radiation Dependence on $T_e$ . . . . .	54
<b>5</b>	<b>Conclusions and Future Work</b>	<b>62</b>

## List of Figures

1.1	Magnetic field configuration in MST . . . . .	2
1.2	Exterior of MST . . . . .	3
1.3	Logarithmic plot of spectrum vs. E. . . . .	5
1.4	Plot of spectrum vs. E with separated lines. . . . .	6
1.5	CSF vs electron temperature profile for simulated plasma . . . . .	7
1.6	CSF vs electron density profile for simulated plasma. . . . .	8
1.7	SXT's lines of sight in MST . . . . .	9
1.8	Exterior of SXT system in MST . . . . .	9
1.9	5 $\mu$ m Al transmission curve . . . . .	11
2.1	Exterior housing of detector. . . . .	16
2.2	Isometric exploded view of the interior housing design. . . . .	17
2.3	0.1in. Fe transmission curve. . . . .	18
2.4	Cross-section of inner housing assembly . . . . .	20
2.5	Diode and filter assembly cross-section . . . . .	20
2.6	Manufactured inner housing parts . . . . .	21
2.7	Test fitting of manufactured inner housing parts. . . . .	22

2.8 Poloidal cross section with detector's lines of sight . . . . .	24
2.9 Poloidal cross section with the intersecting area of the detector's lines of sight	25
3.1 Uniform 5 $\mu\text{m}$ filter thickness transmission curves for Al, Si, and Zr. . . . .	30
3.2 Uniform 5 $\mu\text{m}$ filter thickness passbands for Al, Si, and Zr . . . . .	30
3.3 Logarithmic plot of spectrum vs. E. . . . .	32
3.4 4.6 $\mu\text{m}$ Be transmission curve . . . . .	33
3.5 Uniform 5 $\mu\text{m}$ total thickness transmission curves for Al, Si, and Zr optimized with Be. . . . .	34
3.6 Uniform 5 $\mu\text{m}$ total thickness passbands for Al, Si, and Zr optimized with Be . . . . .	34
3.7 Limits of figure of merit. . . . .	36
3.8 Theoretically optimal transmission curves for Al, Si, and Zr with Be. . . . .	37
3.9 Theoretically optimal passbands for Al, Si, and Zr with Be . . . . .	38
3.10 Realizable optimal transmission curves for Al, Si, and Zr with Be. . . . .	39
3.11 Final design passbands for Al, Si, and Zr with Be . . . . .	40
3.12 Final design 3-passband application . . . . .	41
3.13 Physical Al, Si, and Zr filters . . . . .	42
4.1 Electron temperature profile for simulated plasma . . . . .	45
4.2 Electron density profile for simulated plasma. . . . .	45
4.3 Filter signal vs $n_e(0)$ . . . . .	47
4.4 Total passbands' signals vs $n_e(0)$ . . . . .	48
4.5 Total passbands' signals vs $n_e(0)$ close-up . . . . .	49
4.6 $T_{\text{Zr}}\text{-}T_{\text{Si}}$ passband's separated signals vs $n_e(0)$ . . . . .	50
4.7 $T_{\text{Si}}\text{-}T_{\text{Al}}$ passband's separated signals vs $n_e(0)$ . . . . .	50

4.8 $T_{Zr-TAl}$ passband's separated signals vs $n_e(0)$ .....	51
4.9 Ratio of line radiation to total signals vs $n_e(0)$ .....	52
4.10 Ratio of $Al^{11+}$ to $Al^{12+}$ line radiation signals vs $n_e(0)$ .....	53
4.11 Filter signal vs $T_e(0)$ .....	54
4.12 Total passbands' signals vs $T_e(0)$ . .....	55
4.13 Total passbands' signals vs $T_e(0)$ close-up. ....	56
4.14 $T_{Zr-TSi}$ passband's separated signals vs $T_e(0)$ .....	57
4.15 $T_{Si-TAl}$ passband's separated signals vs $T_e(0)$ . ....	57
4.16 $T_{Zr-TAl}$ passband's separated signals vs $T_e(0)$ .....	58
4.17 Ratio of line radiation to total signals vs $T_e(0)$ .....	59
4.18 Ratio of $Al^{11+}$ to $Al^{12+}$ line radiation signals vs $T_e(0)$ .....	60
4.19 Ratio of $T_{Zr-TSi}$ to $T_{Si-TAl}$ passbands' total signals vs $T_e(0)$ .....	61

# Chapter 1

## Introduction

By utilizing plasma diagnostics, we can delve into the mysteries of that which fuels the light in our universe, fusion. We seek to study this energy source by using diagnostics to measure the behavior of the plasma. Diagnostics allow us to observe and quantify the characteristics of the plasma and, as a result, infer why the plasma possesses them. By measuring the behavior of the plasma and understanding why it has such qualities, we improve our understanding of plasma confinement, in turn, advancing towards a greater possibility of sustaining fusion for positive energy generation.

When utilized alone, every diagnostic has its constraints, but, when their measurements are utilized in conjunction with those of other diagnostics, their capabilities are greatly improved. We shall see this with one notable diagnostic of interest, the Soft X-ray Tomography (SXT)

system designed to measure electron temperature, which does not account for line radiation in its measurements in MST.

This thesis describes the design and expected results from the development of an Al line radiation spectrometer, named the NICKAL2 detector. The first chapter provides an overview of Madison Symmetric Torus (MST) and its magnetic field structure (1.1), explains the various types of electromagnetic x-rays (1.2), describes the currently-used process of the double-filter technique (1.3), gives a basic overview of spectral filters (1.4), and delves into the constraints imposed by the double-filter technique (1.5). 1.6 provides an overview of the remaining thesis sections.

## 1.1 Introduction to the Madison Symmetric Torus

The MST is a fusion plasma physics experiment. MST utilizes a reversed field pinch (RFP) magnetic confinement configuration [Figure 1.1]. Due to this configuration, MST has a unique magnetic field structure.

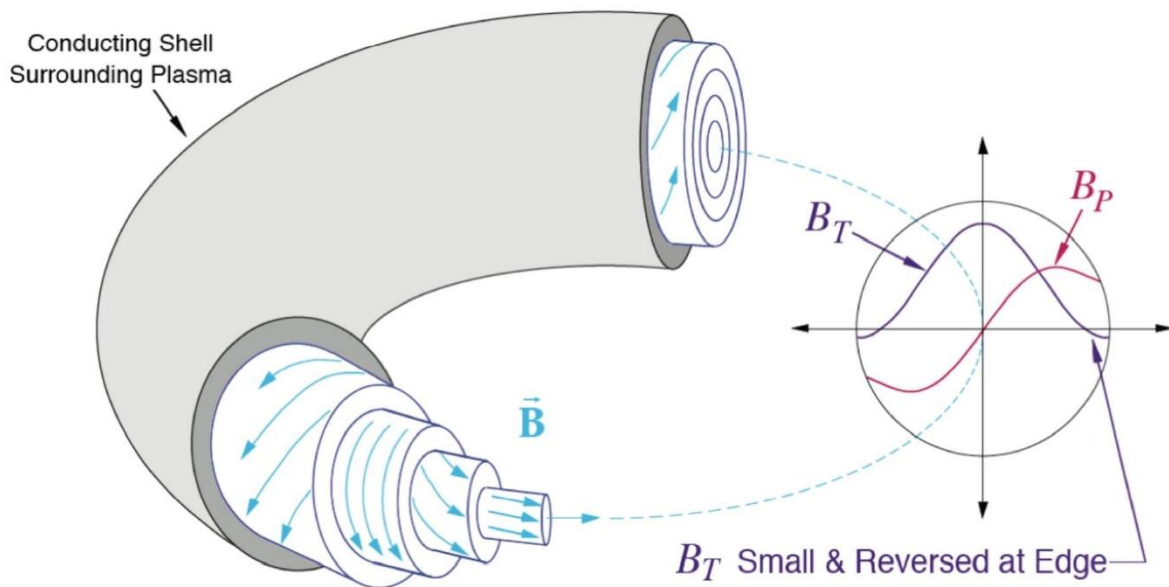


Figure 1.1: RFP magnetic field configuration of MST. The toroidal magnetic field reverses directions at the edge of the plasma. [1]

The toroidal magnetic field of the plasma reverses direction near the edge. The topology of the internal magnetic field influences the confinement of the electrons and ions because the particles travel along the field lines much more easily than across them. Manipulating the magnetic field profile can alter the particle confinement of the plasma and, more specifically, this thesis' main plasma parameters of interest: electron temperature ( $T_e$ ) and electron density ( $n_e$ ).

MST plasmas are contained within a close-fitting, conducting, aluminum vacuum vessel. As a result, aluminum impurities are produced and become confined within the plasma. When atoms, such as aluminum and its charge states, interact with free electrons in the plasma, they can produce x-ray radiation and complicate our current diagnostic measurements and, in turn, our understanding of the plasma.

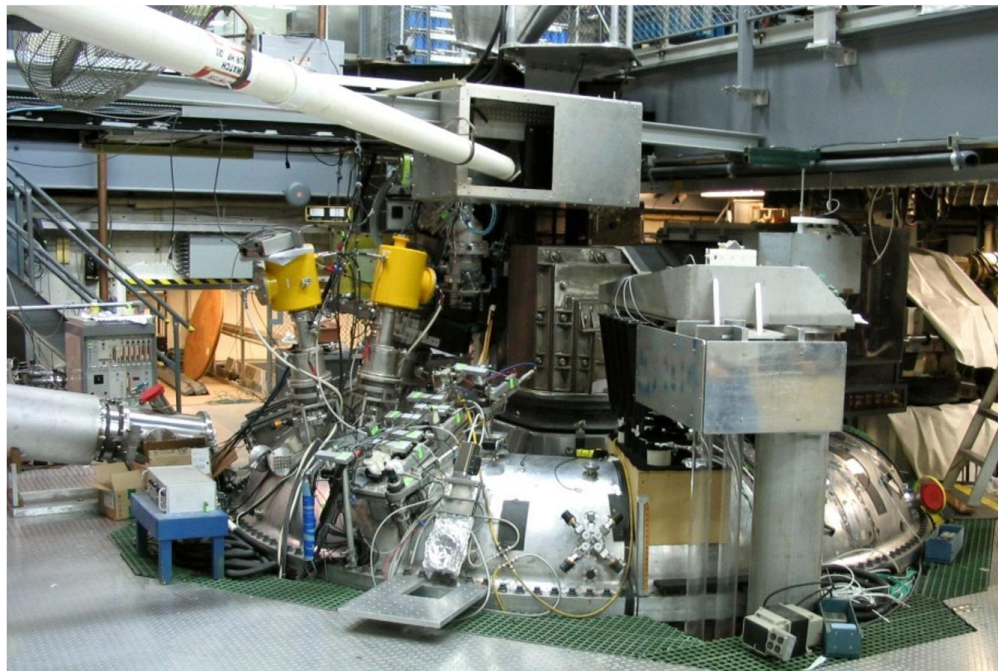


Figure 1.2: Exterior of MST

## 1.2 X-ray Radiation in MST Plasmas

X-ray emissions of MST are a valuable source for diagnosing the inner workings of the plasma. They allow us to better understand the various characteristic plasma profiles and, as a result, its magnetic field configuration and confinement properties. In the specific case of the NICKAL2 detector, they allow us to develop a tool to more accurately measure and understand the electron temperature profile of MST plasmas. Because electrons mostly travel along magnetic field lines and emit x-rays, we can learn about the confinement properties of a plasma by studying these x-rays. Three major types of electromagnetic radiation occur that produce soft x-rays in MST: bremsstrahlung, recombination, and line radiation.

The most common radiation in MST is bremsstrahlung, or free-free, radiation. This occurs due to the many high-energy, free electrons moving past ions. The electromagnetic force between the negative electron and positive nucleus results in a decelerating force on the electron. In order to conserve energy, a photon is emitted equal in energy to that which was lost by the electron. This form of radiation is the background radiation that produces the continuum in MST plasmas.

The second type of radiation occurring in MST is radiative recombination. In radiative recombination, a positively charged ion captures a free electron within one of its bound orbits, emitting a photon equal in energy to the excess energy of the original electron. Recombination radiation appears as a step in the spectrum at an energy equal to the ionization energy of the atom [Figure 1.3]. Recombination is often considered part of the continuum due to the electron originally being free and, therefore, coming from the continuum.

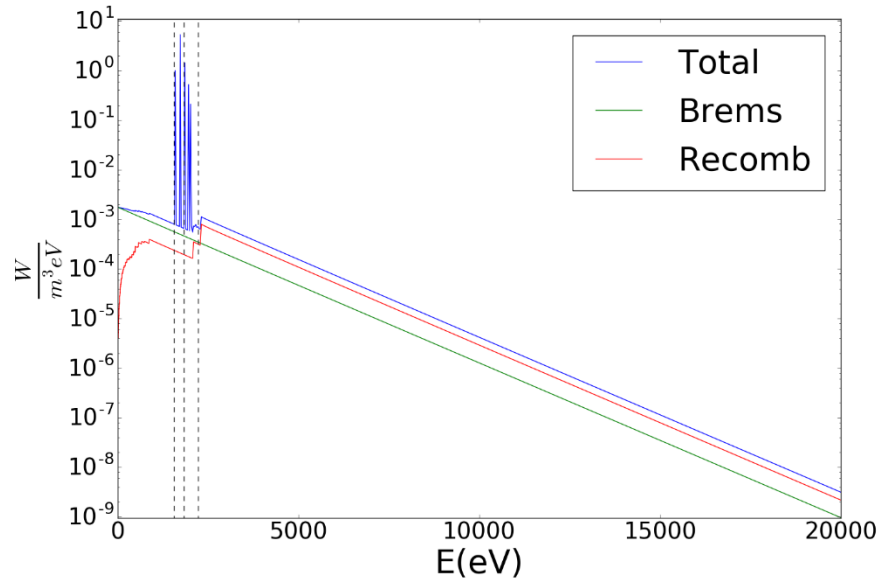


Figure 1.3: Logarithmic plot of a simulated plasma spectrum as a function of energy. The emissions are separated into those from the bremsstrahlung (green), recombination (red), and total radiation (blue). The dashed lines are at 1.5 and 2.1 keV, localizing the line radiation. Plasma parameters  $T_e=1.4\text{keV}$ ,  $n_e=0.013 \times 10^{19} \text{ m}^{-3}$ ,  $n_A=0.00108 \times 10^{19} \text{ m}^{-3}$ .  $n_e=0.013 \times 10^{19} \text{ m}^{-3}$  is not realistic in MST. It was chosen to clearly show the recombination step.

The final type of x-ray radiation originates from line radiation, consisting of elemental emission lines. Due to collisions, bound electrons absorb energy to excite to a higher quantum energy level. Over time, the electrons decay back to lower energy states. Upon an electron lowering in energy level, a photon is emitted, accounting for the energy difference in states. The line radiation measured consists of the accumulation of the emitted photons.

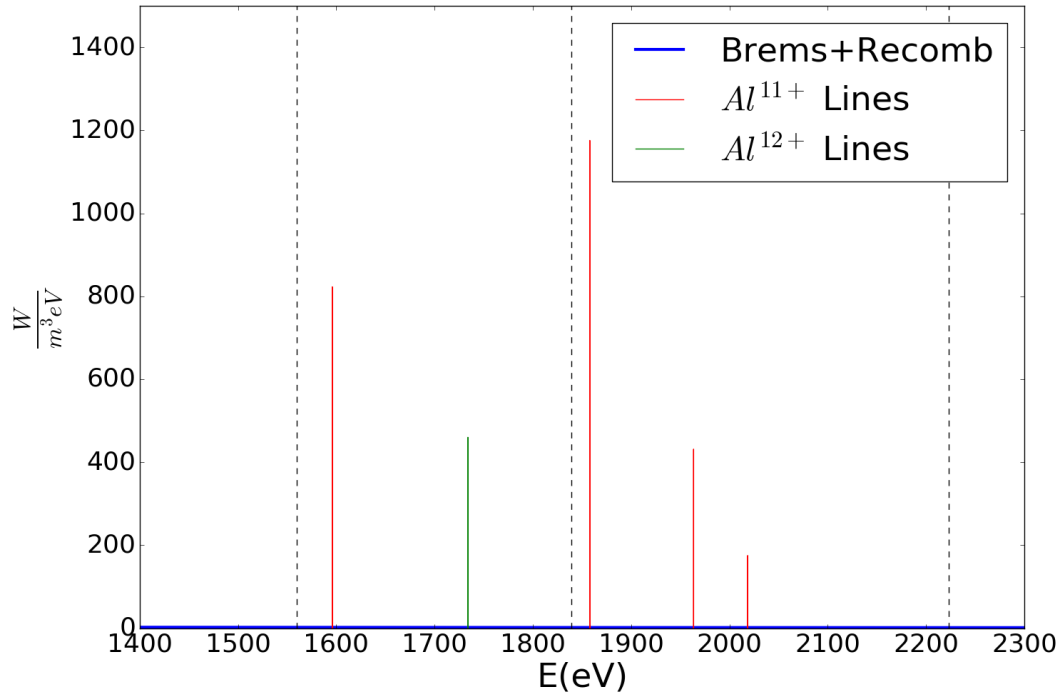


Figure 1.4: Plot of a  $T_e=1.4$  keV plasma spectrum as a function of energy. The lines of each charge state are separated from the continuum emissions. The dashed lines are at 1559.6eV, 1849eV, and 2223eV, localizing the line radiation. The blue line is the total bremsstrahlung and recombination radiation. Plasma parameters :  $T_e=1.4$ keV,  $n_e=1.13 \times 10^{19} \text{ m}^{-3}$ ,  $n_{\text{Al}}=0.00108 \times 10^{19} \text{ m}^{-3}$

Line radiation can occur due to any atom. In our case, the extremely bright Al lines in MST are the cause for concern. Al has many emission lines, which occur throughout the UV and X-ray energy spectra. We are primarily concerned with soft x-rays, so we use filters to filter out optical and UV photons.  $\text{Al}^{11+}$  and  $\text{Al}^{12+}$  are the only charge states that have emission lines in the soft x-ray range of energies. The vast majority of brightness from Al lines that we see in the SXR spectrum originates from a few select lines of the  $\text{Al}^{11+}$  and  $\text{Al}^{12+}$  charge states. The brightest  $\text{Al}^{12+}$  lines occur at 1729.21eV, 2049.33eV, 2160.00eV, and 2214.00eV, and the brightest  $\text{Al}^{11+}$  lines occur at 1599.80eV, 1870.05eV, 1964.88eV, 1964.88eV, and 2009.47eV. The aforementioned lines account for the vast majority of the x-ray radiation brightness seen in MST.

As a result, these are the only Al lines that are incorporated in the spectrum calculations for the filter development in Chapter 3.

In addition, these lines do not always appear in the emission spectrum of a simulated plasma due to their negligible brightness contribution. The probability of Al atoms being ionized is proportional to electron temperature,  $T_e$ , and electron density,  $n_e$ . As electrons become more abundant in a space of constant volume and temperature, the probability of collisions and, therefore, transitions should increase. Likewise, as  $T_e$  increases with the electron density held constant, electrons are more likely to excite Al atoms to higher charge states. In our case, some  $Al^{11+}$  and  $Al^{12+}$  lines do not appear in the spectrum simulations because of the lower  $T_e$  range that we focused on.

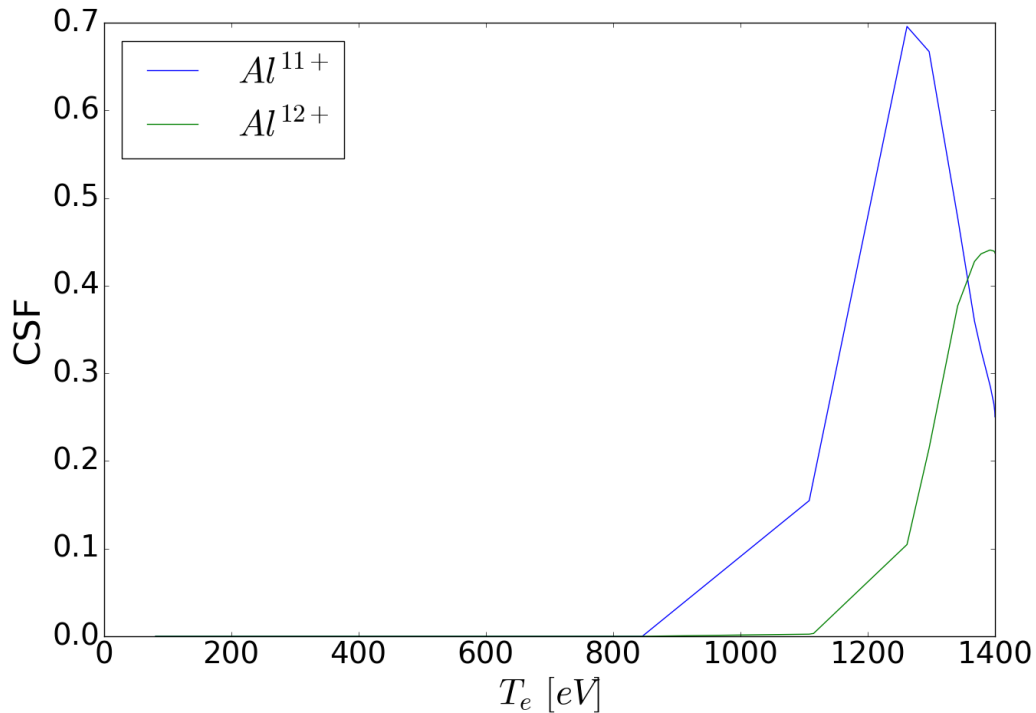


Figure 1.5: Charge state fraction of the  $Al^{11+}$  and  $Al^{12+}$  charge states as a function of the temperature profile of MST. Plasma parameters :  $T_e=1.4\text{keV}$ ,  $n_e=1.13\times 10^{19}\text{ m}^{-3}$ ,  $n_{Al}=0.00108\times 10^{19}\text{ m}^{-3}$

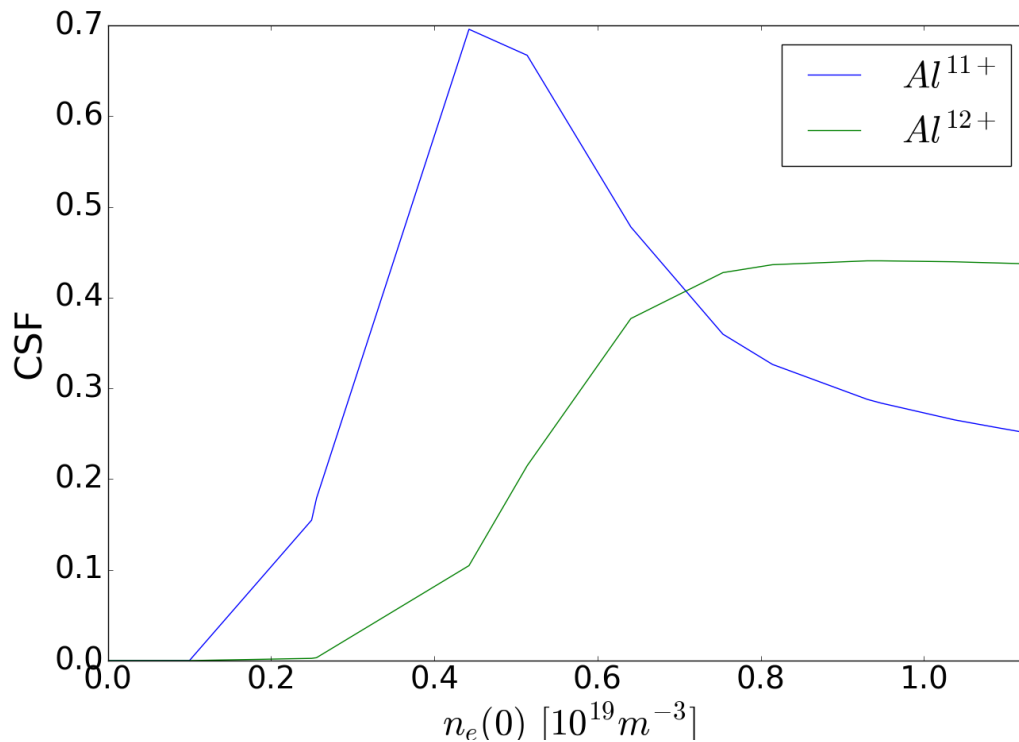


Figure 1.6: Charge state fraction of the  $Al^{11+}$  and  $Al^{12+}$  charge states as a function of the electron density profile of MST. Plasma parameters :  $T_e=1.4keV$ ,  $n_e=1.13 \times 10^{19} m^{-3}$ ,  $n_{Al}=0.00108 \times 10^{19} m^{-3}$ , core neutral density= $1.0 \times 10^{14} m^{-3}$

### 1.3 Two-Color Technique

If we understand the general behavior of the density and emission spectrum of the plasma, we can utilize the two-color technique. The SXR tomography (SXT) system on MST has four cameras, each with ten lines of sight viewing the plasma. Each camera has 20 diodes with two diodes taking measurements along each line of sight. Therefore, each of these detector pairs view the same approximate region of the plasma, so the plasma parameters vary in the same way, allowing the two-color technique to be performed [Figure 1.7]. The two-color technique uses the ratio of SXR signals from two filtered detectors with lines of sight observing the same location in the plasma to infer  $T_e$ .

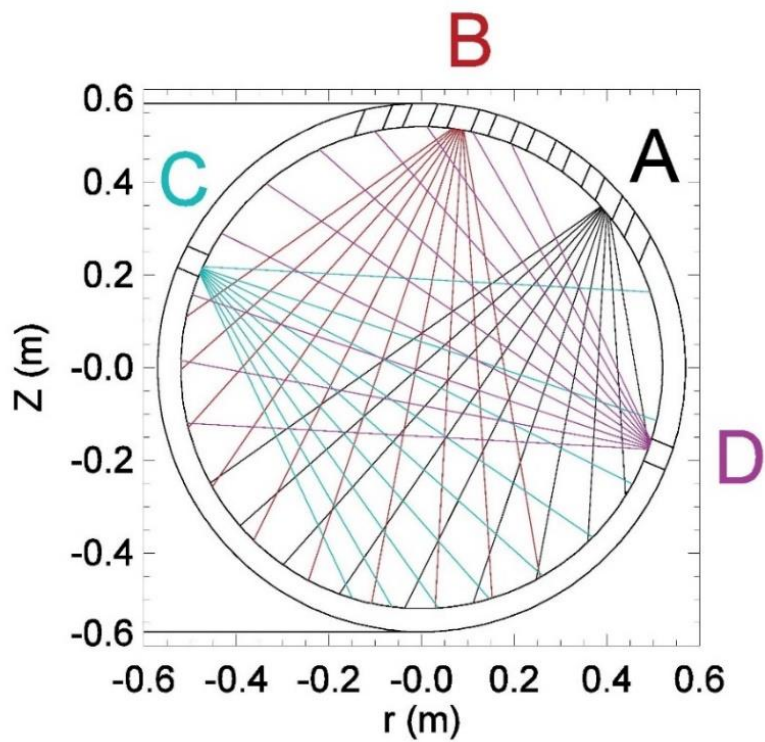


Figure 1.7: Lines of sight of the two-color technique detectors for the SXT (Soft X-ray Tomography) system on MST.

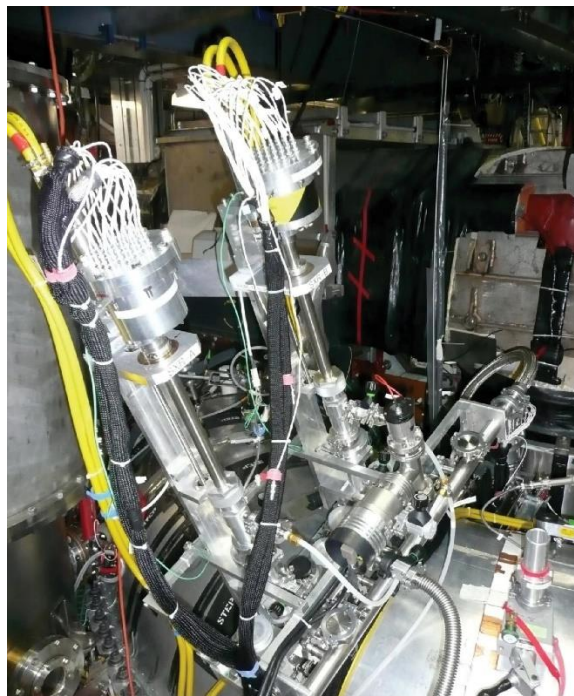


Figure 1.8: Exterior view of the detectors that use the two-color technique in the SXT system.

A plasma must have only bremsstrahlung continuum and a Maxwellian electron distribution in order for this technique to be performed accurately [2]. Due to the different thickness filters, different signals will be measured, which, in turn, can be used to experimentally determine  $T_e$ . The emissivity measured by each detector is given by:

$$\epsilon_{obs} = K \int_E dE A(E)T(E, x) \left\{ \frac{Z_{eff} n_e^2(r)}{\sqrt{T_e(r)}} e^{-\frac{E}{T_e(r)}} \right\} \quad (1.1)$$

$K$  is a constant.  $A(E)$  is the absorption of the detector and  $T(E)$  is the transmission of the filter with a thickness of  $x$ . Both are functions of energy. The portion in brackets is the bremsstrahlung signal from a Maxwell-Boltzmann electron distribution.  $n_e$  is the electron density, and  $n_e$  and  $T_e$  are functions of spatial location, not of energy [1]. The total emissivity integrated over the observed path  $L$  is expressed as:

$$S_i(L) = \int_L dL \epsilon_i \quad (1.2)$$

$S_i$ , where  $i$  denotes either detector 1 or 2, is the signal measured by either detector. The temperature is not a line-integrated quantity, so we cannot separate it into local components from regions along the line of sight. Instead,  $T_e$  represents the highest electron temperature along the line of sight of the detector [1]. The ratio of the signals is:

$$R = \frac{S_1}{S_2} = \frac{\int_L \epsilon_1(T_e) d\vec{L}}{\int_L \epsilon_2(T_e) d\vec{L}} \quad (1.3)$$

This ratio of experimentally measured values is then used to calculate  $T_e$ . When performing the line integral, each diode pair shares a line of sight, resulting in the spatial dependence being pulled out of the integral and cancelling in the ratio. Simplifying eq 1.1, we obtain:

$$R = \frac{S_1}{S_2} = \frac{\int_L \int_E dE A_1(E)T_1(E, x) \left\{ e^{-\frac{E}{T_e(r)}} \right\} dr}{\int_L \int_E dE A_2(E)T_2(E, x) \left\{ e^{-\frac{E}{T_e(r)}} \right\} dr} \quad (1.4)$$

Therefore,  $R$  is determined by the absorption of each detector, the transmission of each filter, and  $T_e$  [1]. Due to knowing the transmission and absorption,  $T_e$  can be determined from  $R$

## 1.4 Optical Filters and Transmission Curves

Both the SXT system and NICKAL2 utilize filtered detectors. By using filtered detectors, the transmission can be manipulated in advantageous ways. Each filter has a transmission curve that varies due to its thickness. There is at least one absorption edge in every transmission curve for each element. Absorption edges are sharp drop-offs in transmission that occur at energies equal to the ionization potential of the filter element. By varying the element and the thickness of the filter, the energy range of photons measured by the detector can be advantageously manipulated. For example, the SXT system utilizes  $>400\mu\text{m}$  Be to make the Al line radiation negligible. As a result of these extreme thicknesses, transmission is significantly lower at the line radiation energies but much higher as energy increases, which is where there is only the continuum. If  $T_e$  is sufficiently large, the continuum will be sufficiently bright to take reliable measurements.

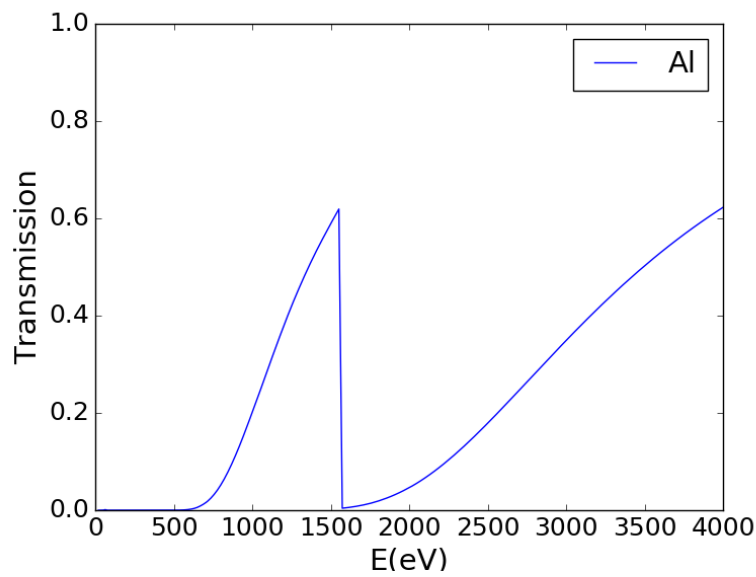


Figure 1.9:  $5.0\mu\text{m}$  Al filter with a K-edge at  $1556\text{eV}$ .

In addition, Be has a low-energy absorption edge, which occurs at 115eV, meaning the transmission curve is smooth and continuous in the x-ray energy range. For most applications, a smooth, continuous transmission curve is desired, such as in the SXT system. This is not the case for the NICKAL2 detector. In the application for NICKAL2, we use elements with K-edges and L-edges. A K-edge occurs at the binding energy of the K-shell electron of the atom, whereas, the L-edge corresponds to the energy that is needed to excite 2p electron to an unoccupied d orbital. Due to there being three different energy quantum states for a single electron in the 2p orbital, there are three L-edges that appear in the transmission curve of any metal. The lowest energy of the three absorption edges, the  $L_{III}$  edge, is the most significant and was the most useful for creating the filter design of NICKAL2. The design of NICKAL2 was based on the manipulation of transmission curves using these absorption edges to selectively transmit only a certain region of the SXR spectrum, in our case, the region containing the Al line radiation.

## 1.5 Motivation

The NICKAL2 detector was designed for measuring Al line radiation signal. To use the SXT system, we essentially assume that the bremsstrahlung continuum is the majority of the spectrum. The SXT system uses the slope of the continuum to measure  $T_e$ , therefore, if the apparent slope is greater than that of the continuum due to line radiation, we run into problems when applying the two-color technique. Looking at Figure 1.3, this problem clearly arises at  $1.59 < E < 2.25 \text{keV}$  where the bright lines occur. Due to the bremsstrahlung continuum assumption of the SXT system, we currently use very thick Be filters ( $>400\mu\text{m}$ ) to make the transmitted line radiation negligible in our measurements. The thick filters constrain our  $T_e$  measurement range due to  $T_e$  being positively correlated with the total signal strength seen in eq (1.1). If we employ

thinner filters, lines contribute significantly to the signal and the assumption of only a bremsstrahlung continuum is violated. By accurately measuring the Al line radiation signal using NICKAL2, we can subtract the signal measured by NICKAL2 from the total SXR signal of the SXT system when the SXT system is using thin filters, preserving the assumption made by the SXT system. Our main goal is to decrease the minimum employable filter thickness and, as a result, the minimum accessible temperature when utilizing the SXT system.

Our secondary goal was to separate the lines of each respective charge state. Within our  $T_e(0)$  range of interest,  $T_e(0) < 1.2 \text{ keV}$ , and typical  $n_e(0)$  range for MST,  $0.1 \times 10^{19} \text{ m}^{-3} < n_e < 1.5 \times 10^{19} \text{ m}^{-3}$ , the 1599.80eV, 1870.05eV, 1964.88eV, and 2009.47eV lines were consistently the only  $\text{Al}^{11+}$  lines that appeared in simulated spectrums. Similarly, the 1729.21eV line was the only  $\text{Al}^{12+}$  line that appeared in simulated spectrums at these parameter ranges. Due to our major interest in the effectiveness of NICKAL2 at  $T_e(0) < 1.0 \text{ keV}$ , there was hope that the line radiation from each respective charge state can be separated. Because the ionization energies of Al are dependent on the available energy, this would make another tool for  $T_e$  analysis.

## 1.6 Thesis Overview

This thesis describes the development of a NICKAL2 detector to measure and potentially separate the line radiation of the  $\text{Al}^{11+}$  and  $\text{Al}^{12+}$  charge states. Chapter 2 summarizes the exterior housing design and assembly process. A description of parts is provided in the order of assembly, with focus on the functionality of the AXUV-20G photodiodes. AXUV-20G diodes are found to have near 100% quantum efficiency where we expect to see high emission. Due to both the efficiency of the detectors and the continuum decreasing as energy increases, the lower efficiency at  $E > 6 \text{ keV}$  is inconsequential. Geometric analysis was done on the lines of sight and

their observable range in the plasma. The intersection of the lines of sight was found to be near the confinement wall, but the overlapping region reaches deep enough into the plasma for our purposes. Precautions that must be taken when assembling and disassembling the interior housing are discussed.

Chapter 3 describes the filter development process. The NICKAL2 design starts from the base idea of a ROSS filter consisting of single-element filters. This design is then expanded upon by incorporating a second, highly transmissive element, beryllium, and optimizing for maximal line radiation signal. Plasmas and filters are modeled using Paolo Franz Model (PFM) [3], which utilizes data from Atomic Data and Analysis Structures (ADAS) [4] for modeling the line radiation and transmission data from the Center for X-ray Optics (CXRO) [5] to determine the expected transmission and signal from various filter configurations. Manufacturing limitations of Si and the uncertainties of the thicknesses are discussed along with their implications.

Chapter 4 discusses the effectiveness of our final design based on simulations using PFM. Simulated signal analysis is performed on our final filter design, focusing on the dependency on  $T_e(0)$  and  $n_e(0)$  for the signal. As predicted by simulations, the expanded temperature range of the SXT system is  $T_e(0) \geq 225\text{eV}$ . The partial separation of charge states is demonstrated. Though not experimentally measurable, the simulated ratio of  $\text{Al}^{11+}$  to  $\text{Al}^{12+}$  line radiation signal as a function of  $T_e(0)$  and  $n_e(0)$  shows dependence of the excitation probability on electron energy and the number of collision targets. Finally, the  $T_e(0)$  range at which the two-color technique can be applied solely to the NICKAL2 detector is discussed.

## Chapter 2

### NICKAL2 Detector: Housing Design

The housing will be re-used from previous work on a Ross filter [Figure 2.1]. This detector has three intersecting lines of sight, one for each filtered detector being used. The detector set-up is contained within the upper chamber, or the inner housing. As a result, this raised the question of whether there would be any major constraints on the inner housing design? These detectors view the plasma through 7 in. long collimators, each with a  $\frac{1}{2}$  in. wide inner diameter. These three collimators are attached to a vacuum pump-out and a CF 2  $\frac{3}{4}$  to KF-50 adapter. This adapter enables the detector to be mounted on the MST Boxport. Due to the large upper chamber, the collimators needed to be angled toward each other, so their lines of sight must intersect. As a result, our second major concern was raised. Would the line of sight geometry be suitable for our measurements?



Figure 2.1 (a) The exterior housing with both the CF 2  $\frac{3}{4}$  to KF 50 and vacuum pump-out attached.

Figure 2.1 (b): A top-down view of the exterior housing. In the uppermost container, the lip on which the outermost O-ring rests is visible. The interior diameter of the lines of sight is visible. Since our diode has a smaller radius for the active area, this does not constrain our design. The housing caps are visible on the lower two containers along with Be filters that are not part of our design.

## 2.1 Inner Housing Design

The initial concern, whether there would be any major constraints on the inner housing design, was easily answered by knowing the dimensions of the commercially available parts. The two pieces that determine this is the vacuum feed-through and the diode that we chose to use. The diodes have a maximum outer diameter of 0.60in. The vacuum feed-through has two important diameters, the maximum diameter of both the head, 0.71 in., and the bolt,  $\sim$ 0.473 in. In addition, the vacuum feed-through has a length of 0.81 in., which is important [6]. Due to the upper chamber having an inner diameter of 0.755 in. and a height of 1.159 in., these commercial

parts easily fit within our re-used housing, leaving suitable room for our remaining components. Concluding that the commercial parts work with the re-used housing, we developed an inner housing design, accounting for the spatial constraints.

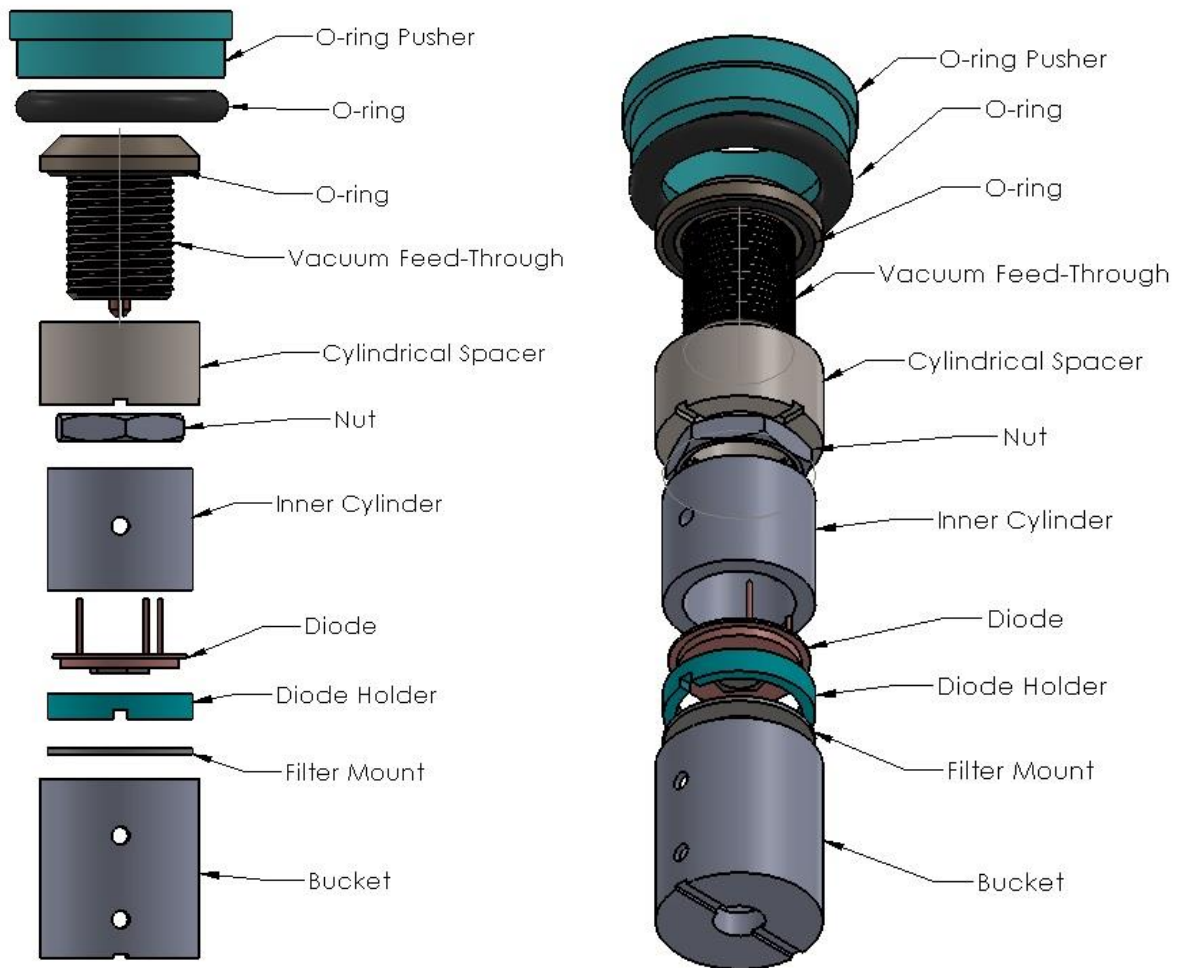


Figure 2.2: Isometric exploded views of the inner housing design and parts.

Going in the assembly order, the first piece is denoted the Bucket. The Bucket serves several functions. First, it restricts the lateral and downward movement of the filter and diode holder. In addition to serving this function, the Bucket acts as a stainless-steel aperture of a minimum 0.1 in. and maximum 0.12 in. thickness due to the ventilation channels. Therefore, it blocks the vast majority of unwanted soft x-rays [Figure 2.3]. The diameter of the aperture

initially was manufactured at 0.222 in., and it will be adjusted downward and re-manufactured as necessary in the event of oversaturation of the diode. Finally, the Bucket allows for easier assembly and insertion of small, fragile parts into the housing.

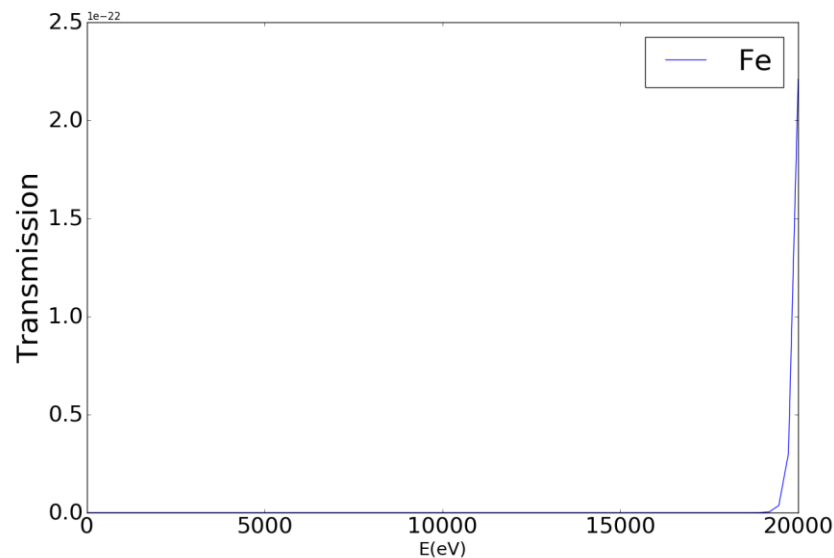


Figure 2.3: Transmission vs E of 2,540  $\mu\text{m}$  (0.10 in.) thick Fe. It is safe to approximate stainless steel as iron. The photodiode detects up to 50 keV, but modeling using CXRO allows for 30 keV max. Clearly, a 0.1 in. thick stainless-steel aperture will block the undesired x-rays. [5]

In order, the four pieces inserted in the Bucket are the filter and mount, the diode holder, the diode, and a cylindrical spacer. The filter mount is a simple, aluminum disk with a 0.420 in. diameter hole, much wider than the aperture. The previous version of a Ross filter had deposited thin films directly onto the diode surface instead of using a separate filter and filter mount. This resulted in transmission that was not in agreement with simulations due to protective layers of material also being deposited on the diode, altering the intended transmission and probably detection. The second piece, the diode holder, is composed of turcite to ensure grounding of the sensitive diode. The diode holder also restricts the movement of the diode, which is pressure-fit in place by the cylindrical spacer. The cylindrical spacer is also composed of

turcite. Ventilation holes are present in both the diode holder and the cylindrical spacer, ensuring there is no residual air pressure on either side of the filter that could pop it during vacuum pumping. The air that is trapped in these regions can easily travel down the wall of the inner housing, under the Bucket, and down the shaft of the detector to the vacuum pump-out at the base [Figure 2.1 (a)].

The diodes utilized are circular AXUV-20G photodiodes produced by International Radiation Detectors, Inc. These diodes have a  $20\text{mm}^2$  active area, making their diameter only slightly smaller than our aperture size. Excluding the variation in active area, the AXUV-20G and AXUV-100G, which is currently produced by Opto-diode, have the same properties [7, 8]. The diodes are designed to measure x-rays from 100 eV to 50 keV [7]. They have a 25-50 $\mu\text{m}$  active Si region thickness [9]. The active Si layer thickness of the diode, estimated as 35 $\mu\text{m}$  for simulation purposes, was accounted for during the filter optimization process. Furthermore, the AXUV-20G diodes possess an 8nm-thick  $\text{SiO}_2$  layer, resulting in near 100% internal quantum efficiency for photons between the energies of 6 and 6000 eV [10]. Due to the thin  $\text{SiO}_2$  layer having negligible effects on x-ray transmission, the  $\text{SiO}_2$  layer was not accounted for when filter optimization was performed. Optimization of the filters accounted for energies of up to 20 keV; whereas, the diode can detect up to 50keV x-rays. Both the absorption and spectrum at higher energies is near zero, so the effect of excluding  $E > 20$  keV x-rays in the optimization is insignificant.

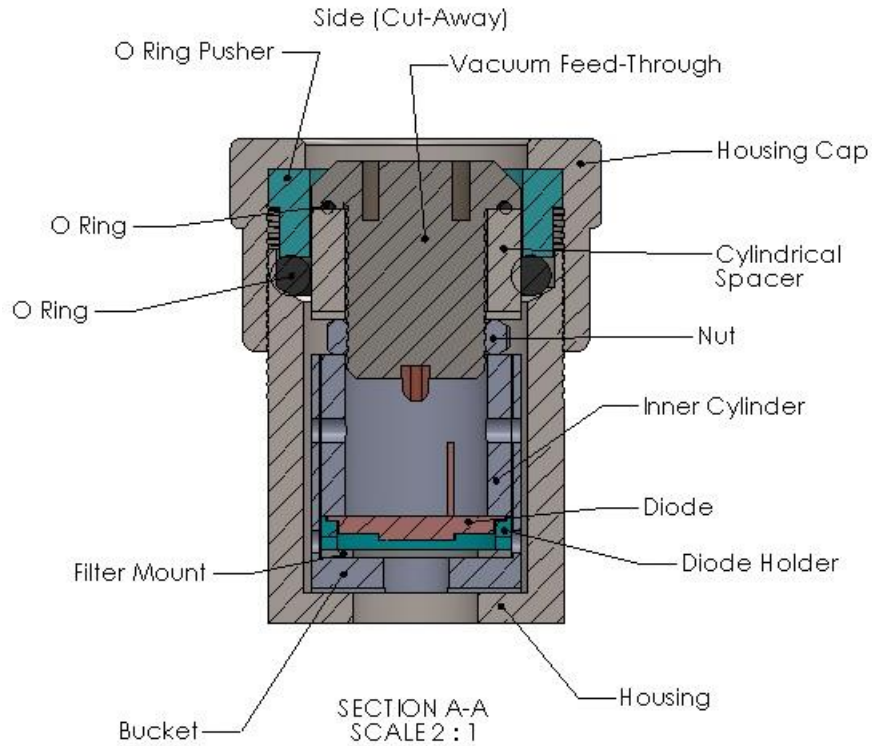


Figure 2.4: Cross section of inner housing assembly

Bottom Half of Side (Cut-Away)

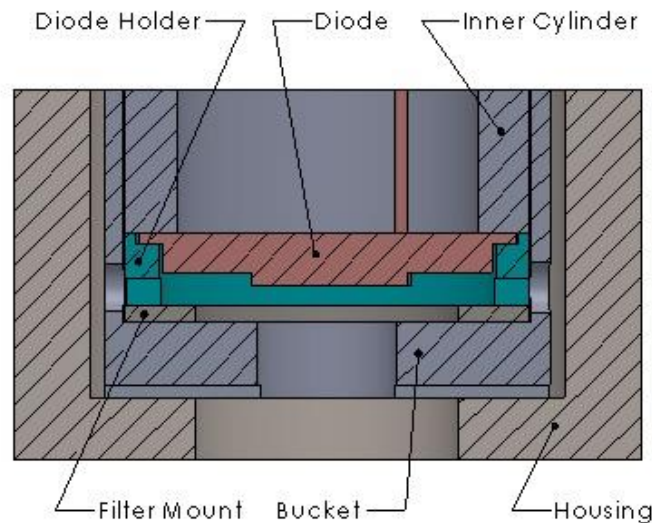


Figure 2.5: Close-up of the diode and filter assembly. There are holes for venting on both sides of the diode and filter to ensure the filter does not pop from the trapped air's pressure. These holes should align when assembling to ensure that the air can escape.

The diode is wired to the vacuum feed-through. The vacuum feed-through is a HGP.0S.302.CLLPV produced by LEMO. Another cylindrical spacer, this one made from aluminum, is placed on the bolt of the vacuum feed-through and held in place with a nut. This sub-assembly will be referred to as the LEMO mechanism. The end of the vacuum feed-through fits within the turcite cylindrical spacer [Figure 2.4]. An O-ring is on the bottom of the head of the vacuum feed-through, and an additional O-ring fits around the aluminum spacer and rests on the lip of the inner housing, with a turcite ring resting on top of that. The housing cap is screwed on, sealing the mechanism. Due to the pressure from the housing cap, both O-rings act on the surface of the aluminum cylindrical spacer. The inner chamber is vacuum-sealed, and the filter and diode set-up are pressure-fit in place by the LEMO mechanism pushing down on them, completing the assembly of the inner chamber.



Figure 2.6: In-house manufactured inner housing components. The opaque white pieces are made from turcite for grounding purposes. The thin aluminum disk is the filter mount. These do not have filters on them and were designed for test fitting purposes due to the fragility of the filters.



Figure 2.7: Test fitting of in-house manufactured components.

Extreme caution must be taken when both assembling and disassembling the detector due to a variety of reasons. The AXUV-20G diode has a total of six fragile, exposed wire bonds on the face of the detector, two connect the white, Si ring surrounding the active area to each anode, cathode, and the ground. A small amount of pressure can break these wire bonds. Secondly, the diodes do not have a thick, protective layer on the active area, and it can be easily scratched. In addition, the filters are thin enough that the force of air currents (i.e. breathing or moving the filter perpendicularly through the air) can pop the filters. All work that must be done when assembling or disassembling the inner housing should be done in a clean, draft-free room with extreme caution. When sealing the inner housing, extreme precaution must be taken to not over-tighten the housing cap, which could break the filter. Next, when pumping out the trapped air in the assembly, one must do it at a very slow and steady rate to ensure the filters do not pop due to a large pressure gradient occurring on either side of them.

## 2.2 Housing Geometry

We re-used the exterior housing from previous work on the Ross filter. As a result, the NICKAL2 detector has three lines of sight that all intersect at the same point. The lines of sight do not necessarily need to intersect for our purposes, but, since the detectors take measurements along the entire line of sight, the detectors do need to be oriented so that they measure approximately the same region of the plasma. Due to the aperture and collimator, the diode measures the line integrated brightness only along a straight line with the width of the aperture. Because of how we measure the Al line radiation (Chapter 3), we ideally want these detectors to take measurements along the same line of sight. Realistically, this was not possible, so each line of sight should have very similar brightness along it. With our physical limitations, the most effective design to do this was one in which the lines of sight intersect somewhere in the plasma. In order to utilize three parallel lines of sight, the area holding our detector components would need to be incredibly small or else all three lines of sight will not be able to see through the KF-50 port on the MST Boxport where the detector will be mounted.

The housing will consist of a three line-of-sight module connected to, with respective heights, a vacuum pump-out [0.50 in.], which is connected to a CF 2  $\frac{3}{4}$  to KF-50 adapter [2.69 in.], produced by Ideal Vacuum Products [11]. The adapter is then installed on the MST Boxport, which possesses a thickness of  $\sim 4$  in., and is located at a toroidal angle of  $90^\circ$ . After installing the detector on MST, the ideal situation would be that these lines of sight intersect at the source of the emission lines, which shifts due to various plasma parameters, in particular  $T_e$  and  $n_e$ . We will see maximum line radiation brightness at that location and, as a result, the signal will consist mostly of that from Al lines. Because of this and the possibility of plasma parameters and brightness spatially varying, we do not want the location where each detector

measures the Al line radiation source to be significantly different from each other. The lines of sight are at an angle of  $88.35^\circ$  from the plane that they are mounted on. Accounting for all of the aforementioned dimensions, the lines of sight intersect at 4.03 in. from the inner wall of the vessel.

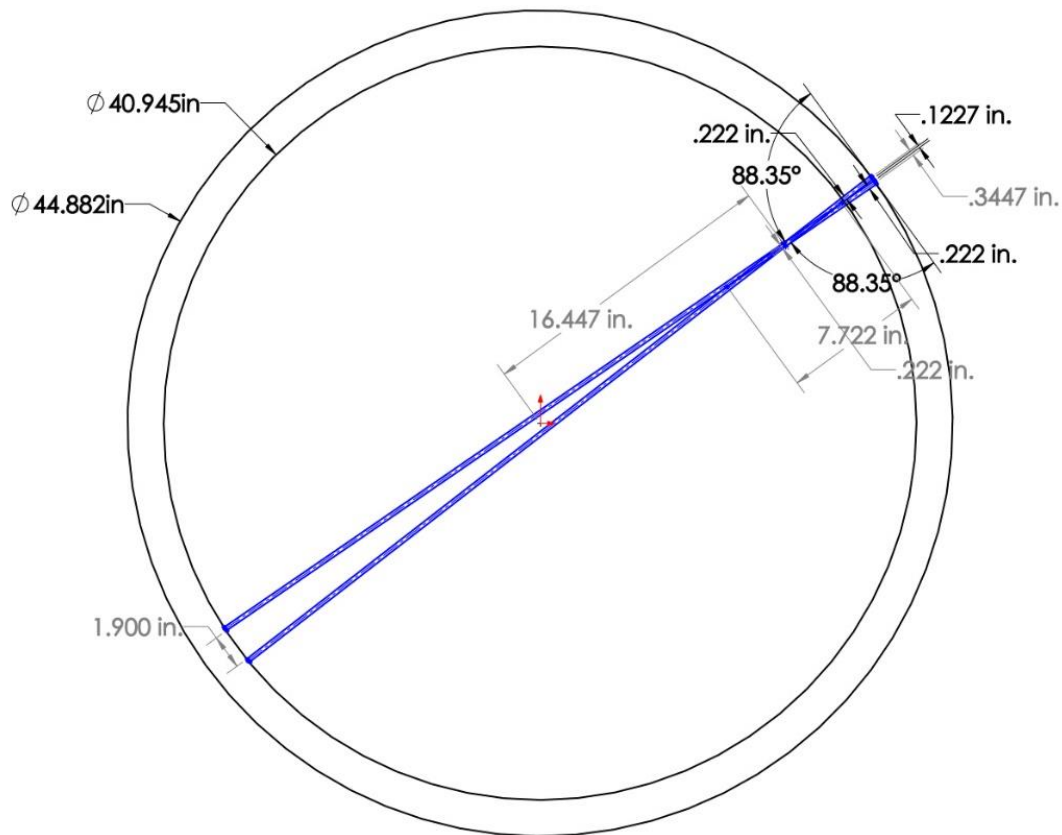


Figure 2.8: Poloidal cross section of MST. The 3.937 in. thick wall is modeled. The blue lines correspond to the edges of the sampling volume of the diodes.

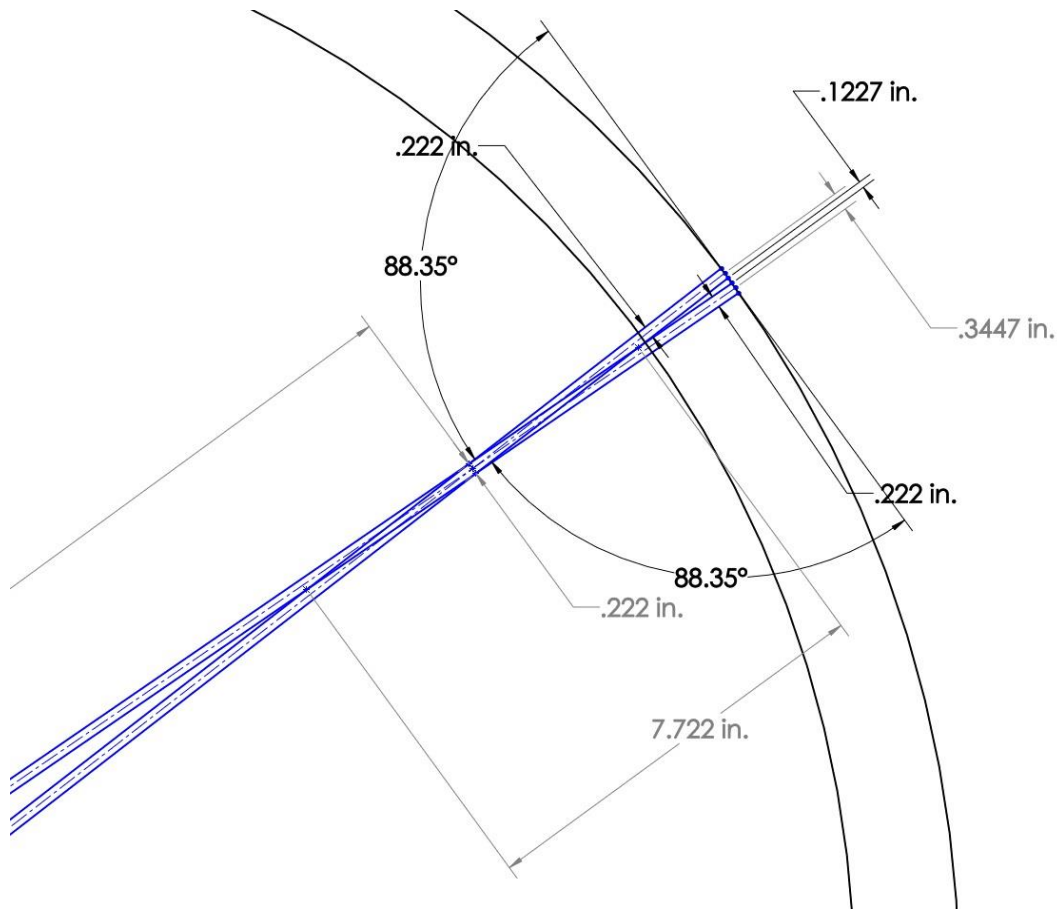


Figure 2.9: Close-up view of the poloidal cross section with mounting geometry near the mounting surface. This diagram accounts for the thickness of the boxport, vacuum pump-out, adapter, and the three lines of sight module, but they are not modelled in the diagram. The dashed line between each pair of solid, blue lines account for treating the lines of sight as pencil beams.

In addition, the overlapping region of our lines of sight is significant because of the 0.222 in.-wide lines of sight due to the aperture and the large angle between each line of sight and the mounting surface [Figure 2.9]. Therefore, the region of overlap has a maximum width of 0.222in., occurring at the point of intersection of the pencil beams. In addition, the region of overlap has a maximum length of 7.722 in, extending 3.861 in. in both directions from center of the intersection for the lines of sight as defined by the pencil beams. Therefore, these detectors have an overlap region of 0.17 in. to 7.89 in. from the inner wall. These 0.222in.-wide lines of sight have a minimum separation distance of 1.90 in. at the opposite wall of the MST. The long

overlap region and small separation at the opposite wall of MST demonstrate that our desire for each line of sight to view the same region of the plasma is satisfied. The overlapping region that each detector measures penetrates a rather large depth into the plasma; therefore, the pre-fabricated housing does satisfy the geometrical constraints.

## Chapter 3

### **NICKAL2 Detector: Filter Design**

In order to take an accurate measurement of the Al line radiation, we would like to confine the majority of measured x-rays to the energy range containing the brightest Al lines. To achieve this, we utilized the transmission curves of various elemental filters and their respective x-ray absorption edges. Each transmission curve has a characteristic x-ray absorption edge that, based on the element, varies at which energy it occurs. These absorption edge energies correspond to the ionization potential of the atom. By taking the difference between two transmission curves of different elements, we can reduce the transmission outside of the two absorption edges greatly while barely influencing that between the edges. [Figure 3.2].

PFM was used for the modelling of all spectra and transmission curves. PFM models plasma profiles and calculates the continuum spectra. Transmission curves and signals were also

modelled using PFM, which accesses transmission data from CXRO[5] and some data for the spectrum calculations from ADAS. ADAS is a collisional-radiative model for the calculation of atomic processes and x-ray emission in astrophysical and fusion plasmas [4]. PFM utilizes data for the charge state fraction and line strength from ADAS to perform the calculation of the line radiation contribution to the spectrum. PFM simulates spectral line radiation by giving these lines a finite but small thickness. Unless otherwise noted, all spectrum simulations use the following plasma parameters:  $T_e=1.4\text{keV}$ ,  $n_e=1.13\times 10^{19}\text{ m}^{-3}$ , and  $n_{\text{Al}}=0.00108\times 10^{19}\text{ m}^{-3}$ .

### 3.1 ROSS Filter

Due to the aforementioned absorption edges, we can create effective ‘spectral bins’, or passbands, where we have large transmission within a certain energy range and significantly reduced transmission elsewhere. This idea and its application on MST initially stemmed from the development of a ROSS filter where the K-edges of elements with smooth transmission curves were used to make a bandpass filter that measures line radiation [12, 13, 14]. The  $\text{Al}^{11+}$  and  $\text{Al}^{12+}$  lines occur between 1.5-2.25 keV, defining our energy range of interest. Therefore, we must choose two elements such that this energy range is contained between the absorption edges of the combination. In addition, we must minimize the spectral width between these two absorption edges while ensuring all the lines are contained within it. This will preserve accuracy by ensuring we are measuring as much of the lines and as little of the background as possible.

The primary purpose of NICKAL2 is to accurately measure the total Al line radiation. In order to achieve this, we only need one passband that contains all of the lines, so we need two filters. For our secondary goal, NICKAL2 should separate the lines of each charge state. There is no clear energy division between the  $\text{Al}^{11+}$  and  $\text{Al}^{12+}$  lines, so we will most likely be unable to completely separate these lines. Although, due to the brightness of the lines varying as a

function of  $T_e$  and  $n_e$ , it may be possible to separate the lines either completely or to an extent at certain ranges of these parameters. Using modeling to achieve both of these goals, we can utilize absorption edges of two elements to contain all of the lines between them and the third absorption line to separate  $Al^{11+}$  and  $Al^{12+}$  lines as much as possible. For the entirety of the filter design process, we focused on the two passbands that should separate the lines of the charge states. If both of these passbands are suitable, the third passband should be as well.

For our purposes, the ideal elements with respective K-edges consist of aluminum (1.562 keV), silicon (1.840 keV), and phosphorous (2.143 keV) [15]. Though the absorption edge of P is not greater than 2.25keV, it is still greater than all simulated lines besides the 2160eV and 2240eV  $Al^{12+}$  lines. These are the dimmest of the simulated  $Al^{12+}$  and do not contribute anything to the simulated signal at  $T_e < 1.2\text{keV}$ . As a result, neglecting to measure these two lines will not significantly impact our measurement.

However, the P filter is unobtainable at purities greater than ~25% due to its combustibility, therefore, the original ROSS filter design was not possible for our needs. K-edges were no longer the realistic ideal, so L-edges were considered as well. The best choice to replace the K-edge of P was zirconium with a  $L_{III}$  x-ray absorption edge at 2.223 keV [15]. The passbands are now  $1.562\text{keV} < E < 1.840\text{keV}$  when signal of Al is subtracted from the signal of Si and  $1.840\text{keV} < E < 2.223\text{keV}$  when the signal of Si is subtracted from that of Zr [Figure 3.2]. Since the lines of sight of the detectors do not spatially vary significantly, we have designed the filters by modelling each detector sharing the same line of sight in PFM. As a result, we can take the difference in the transmission curves of filters to get a passband transmission that, when a single measurement along the line of sight is taken using this transmission difference, the resulting signal should be approximately the same as the experimentally measured signal of the

passband. The experimentally measured signal is acquired by taking the difference between the measured signal of the two corresponding filtered detectors. We go through the process of optimizing this transmission difference in this chapter.

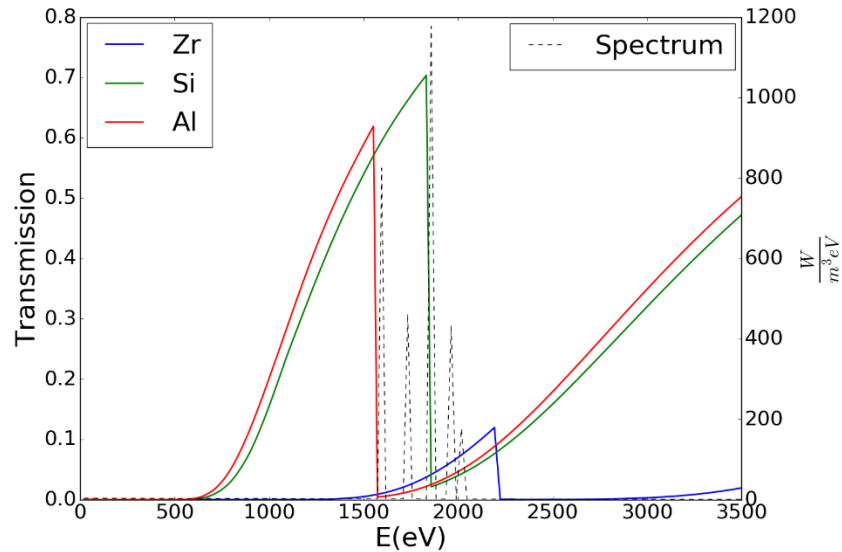


Figure 3.1: Plot of single filter transmission curves vs  $E(\text{eV})$  with a simulated x-ray spectrum. Design consists of three constant, one element filters ( $5.0\mu\text{m}$  Zr,  $5.0\mu\text{m}$  Al,  $5.0\mu\text{m}$  Si). Filter design:  $5.0\mu\text{m}$  Zr,  $5.0\mu\text{m}$  Al,  $5.0\mu\text{m}$  Si

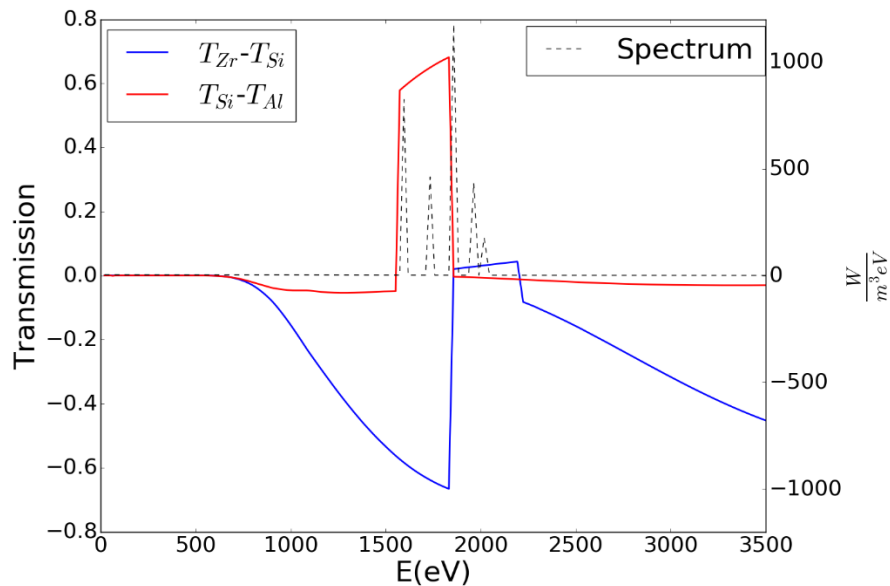


Figure 3.2: Plot of transmission of passbands vs  $E(\text{eV})$  with the x-ray spectrum. Filter design:  $5.0\mu\text{m}$  Zr,  $5.0\mu\text{m}$  Al,  $5.0\mu\text{m}$  Si. On this and the following plots, negative transmission is not possible. It just shows poor transmission matching between the filters.

## 3.2 General Design

For each filter pair, transmission curves must be similar in both general shape and amplitude outside the energy range of each passband, severely restricting the ideal thickness of Zr. Zr is not as transmissive as Al and Si, so at higher thicknesses ( $>3.0\mu\text{m}$ ), the transmission is too low to get a high enough signal. In addition, at very small thicknesses ( $<1.0\mu\text{m}$ ), the absorption edge of Zr does not descend near zero, resulting in the need for extremely thin Al and Si filters. Because of the thickness constraints, the Zr filter must have a relatively small peak transmission compared to P. The change to Zr significantly reduces the maximum transmission of the  $T_{\text{Zr}}\text{-}T_{\text{Si}}$  passband, but, as can be seen in Figure 3.2, the emission of the Al lines contained in  $T_{\text{Zr}}\text{-}T_{\text{Si}}$  dominates the overall continuum. As a result, the change to Zr is inconsequential for our application. In addition, due to the L-series having three absorption edges, there are two small transmission peaks at the  $L_{\text{I}}$ (2.535 keV) and  $L_{\text{II}}$  (2.305 keV) absorption edges. Looking at the soft x-ray spectrum of a simulated MST plasma [Figure 3.3], we see that the amplitude of the continuum at  $E>2.223$  keV is near negligible when compared to that of the lines. As a result, the small increase in transmission within this region results in an inconsequential increase in undesirable signal.

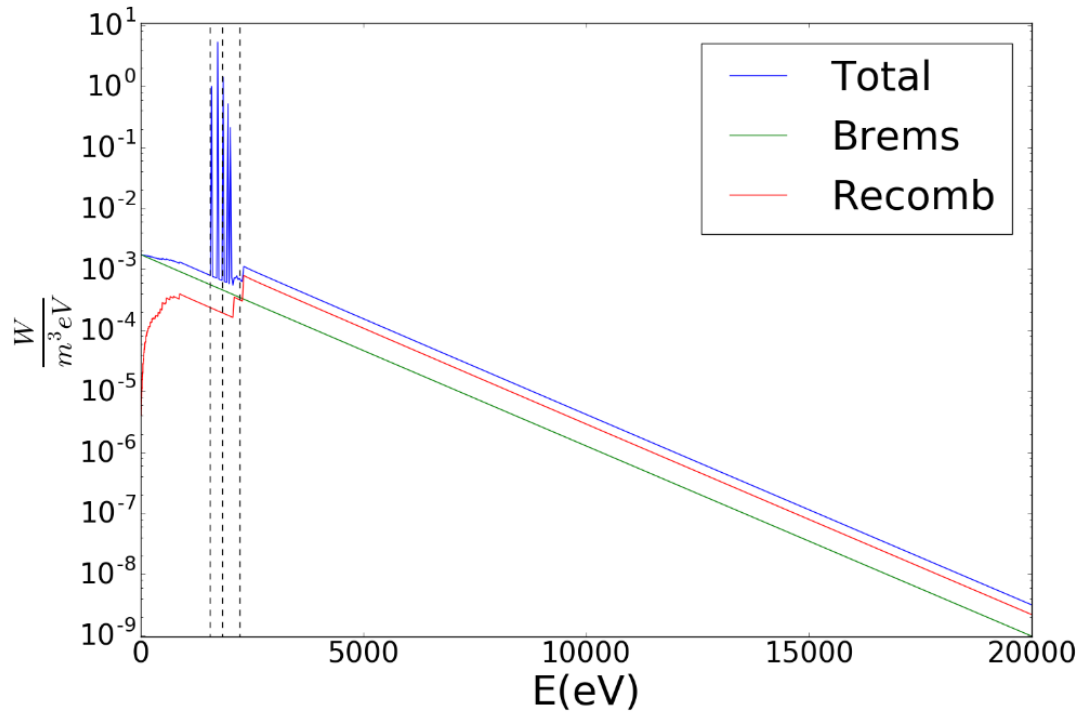


Figure 3.3: Logarithmic plot of a simulated plasma spectrum as a function of energy. The emissions are separated into those from the bremsstrahlung (green), recombination (red), and total radiation (blue). The dashed lines are at 1.5 and 2.1 keV, localizing the line radiation. Plasma parameters  $T_e=1.4\text{keV}$ ,  $n_e=0.013 \times 10^{19} \text{ m}^{-3}$ ,  $n_{Al}=0.00108 \times 10^{19} \text{ m}^{-3}$ .  $n_e=0.013 \times 10^{19} \text{ m}^{-3}$  is not realistic in MST. It was chosen to clearly show the recombination step.

To maximize the relative contribution of line radiation to the signal of each passband, we can include a secondary, highly transmissive element in each filter. Be was chosen for our purposes due to the continuously high and smooth transmission, its common use in filters, and its ability to be deposited as a thin film on Al, Si, and Zr [Figure 3.4].

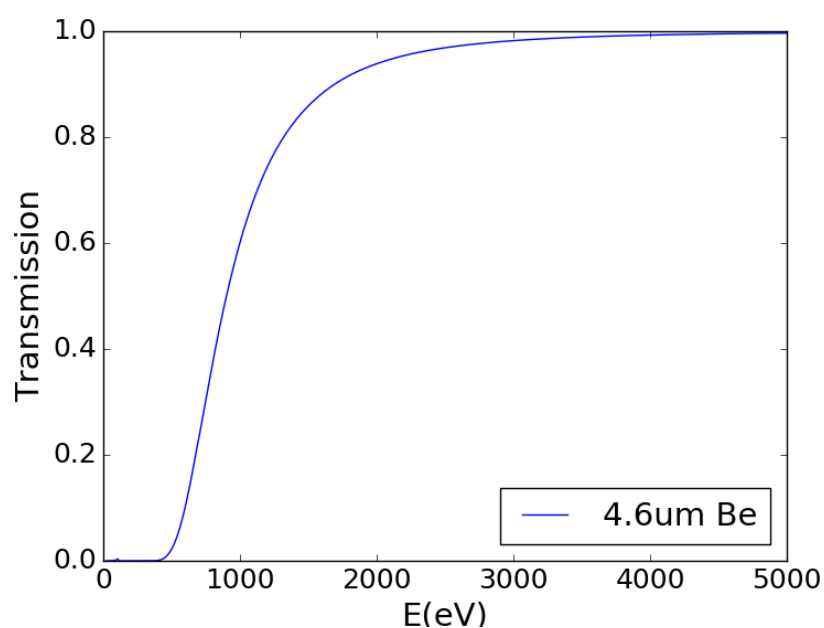


Figure 3.4: Transmission curve for pure Be at 4.6 $\mu\text{m}$  thick. This is the same thickness as used in the following example [Figures 3.5 and 3.6]. [5]

The addition of a thin layer of Be not only increases the transmission within the passband, but also increases the transmission everywhere else. Due to Be having the ability to possess monotonically and nonlinearly increasing transmission at energies greater than its very low K-edge (115eV), we disproportionately manipulated the transmission of our filters at different energies. Secondly, Be is a very transmissive element. Due to Be having the ability to obtain near 100% transmission around our passband energies at reasonably large thicknesses, there is a wide range of Be layer thicknesses that can be used when manipulating the transmission curves of the filters. As a result of these two factors, we can effectively equalize the transmission of each filter to create more ideal passbands. Without the use of Be, the filter design would transmit too much continuum emissions outside of the 1.5-2.25keV range, resulting in our design specification of measured signal consisting entirely of Al lines failing to uphold. Maintaining a uniform 5.0 $\mu\text{m}$  total thickness, the optimal filter design became:

1st Filter: 0.4 $\mu\text{m}$  Zr with 4.6 $\mu\text{m}$  Be

2nd Filter: 5.0 $\mu\text{m}$  Al

3rd Filter: 5.0 $\mu\text{m}$  Si

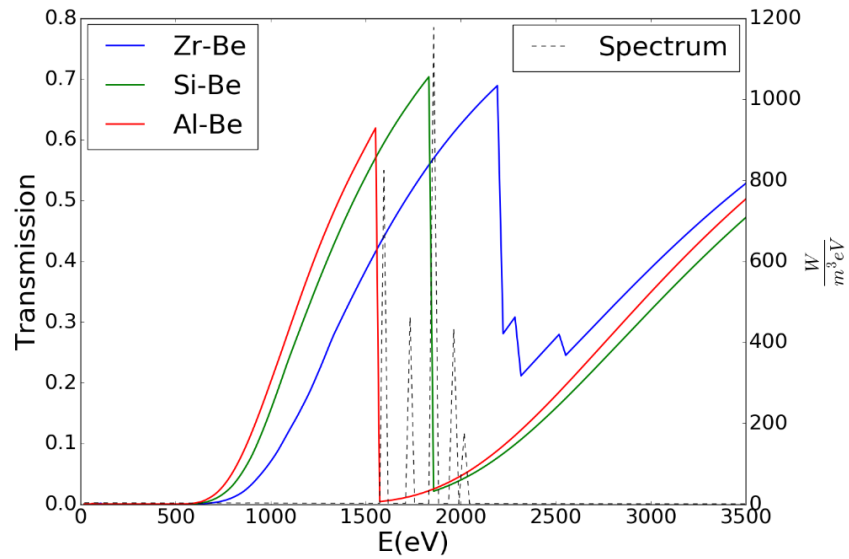


Figure 3.5: Plot of single filter transmission curves vs  $E(\text{eV})$  with a simulated x-ray spectrum. Filter design: 0.4 $\mu\text{m}$  Zr with 4.6 $\mu\text{m}$  Be, 5.0 $\mu\text{m}$  Al, 5.0 $\mu\text{m}$  Si

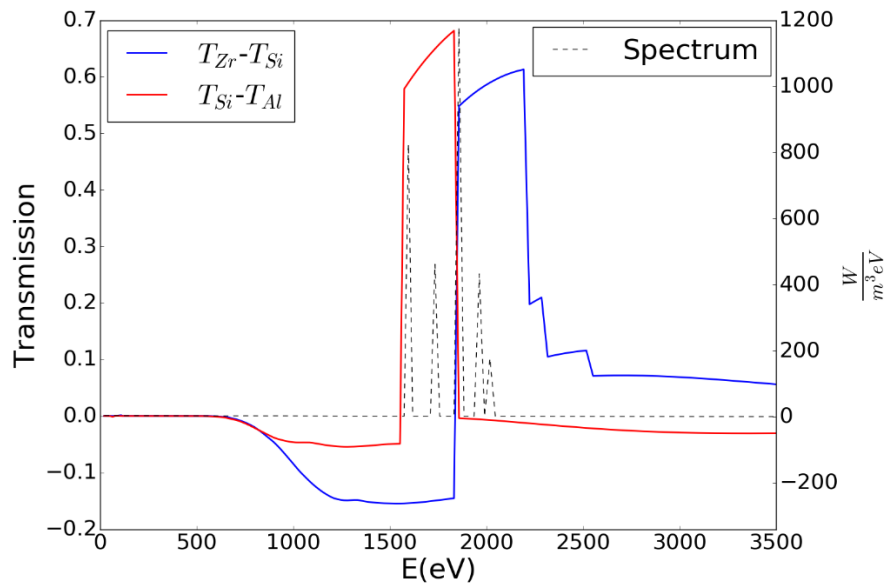


Figure 3.6: Plot of transmission of passbands vs  $E(\text{eV})$  with a simulated x-ray spectrum. The two passbands are  $T_{Zr-T_{Si}}$  (Blue) and  $T_{Si-T_{Al}}$  (Red). Filter design: 0.4 $\mu\text{m}$  Zr with 4.6 $\mu\text{m}$  Be, 5.0 $\mu\text{m}$  Al, 5.0 $\mu\text{m}$  Si

As can be seen in Figure 3.6, the filter design has improved significantly. Maximum transmission of both passbands has increased and that of  $T_{Zr-T_{Si}}$  has increased by at least a factor

of 10. Undesirable transmission outside of the passbands has decreased as well. There was one important region of transmission that needs to be improved for our design to work, that of the  $T_{Zr}-T_{Si}$  passband within the  $T_{Si}-T_{Al}$  passband ( $1.562\text{keV} < E < 1.840\text{keV}$ ). Even with  $T(E) \approx 0.1$ , non-negligible, undesirable signal would be measured due to the massive brightness of the line radiation within this region. In order to have an effective design for separating each respective lines of each charge state, transmission from one passband should be minimal in the energy range of the other passband. Knowing the qualities that we had to look for in our passband filter, we developed an optimization routine.

### 3.3 Optimization Process

Due to the former design being optimized with the constraint of each filter having a  $5.0\mu\text{m}$  total thickness, the final result could be improved even more. As a result, we have designed a figure of merit for this purpose. Knowing the six variables (the thickness of each of the two elements in all three filters), we utilized an optimization routine to determine the ideal composition. First, the following figure of merit was created to quantify the practicality of the configuration:

$$F_i = \frac{\int_{EL_i}^{ER_i} dE \epsilon(E) |T_i(E)|}{\int_0^{EL_i} dE \epsilon(E) |T_i(E)| + \int_{ER_i}^{\infty} dE \epsilon(E) |T_i(E)|} = \frac{\text{Signal within passband}}{\text{Signal outside of passband}} \quad (3.1)$$

$$M_m = F_1 \cdot F_2 \quad (3.2)$$

where  $i$  designates which passband,  $\epsilon(E)$  is the spectral emission, and  $T_i(E)$  is the transmission of the respective passband. The figure of merit is weighted against the spectrum. It favors larger spectral emissions within and punishes that which is outside each respective passband. Because of this quality, our figure of merit severely punishes any transmission cross-over within the passbands. In addition, it accounts for the changing background emission. In a general sense,

due to the decreasing background emissions as the energy of photons increases, the metric favors an equal, non-zero transmission at  $E > ER_i$  more than at  $E < EL_i$ .

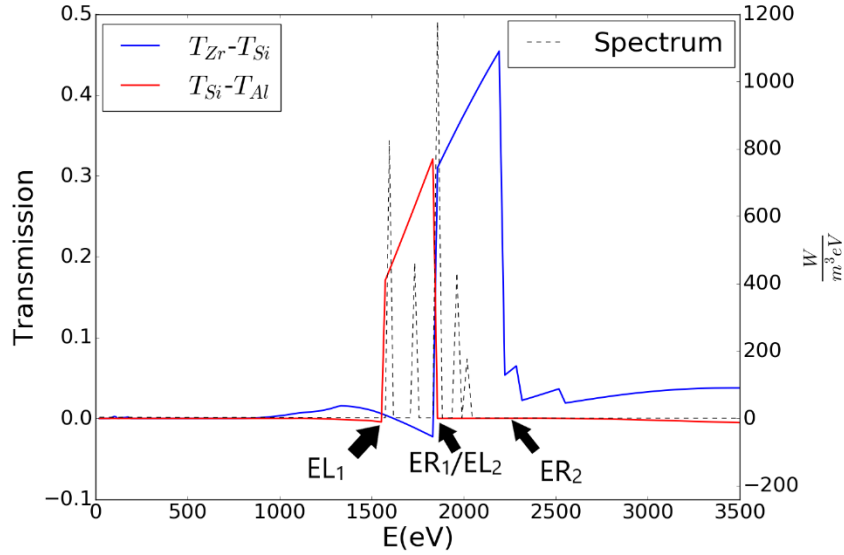


Figure 3.7: The energy limits of the integrals in  $F_i$  are shown. Each respective  $EL_i$  corresponds to the minimum energy value of the passband, whereas,  $ER_i$  denotes the maximum energy of the passband. The first passband corresponds to the  $T_{Si}-T_{Al}$  passband.

Secondly, we divided the signal in the passband by the signal outside of it. This was to ensure we maintain the positive output we had desired. If we had subtracted the signal outside of the passband from that within it, we would have had the potential to obtain a negative result. If this were true for both passbands, our metric,  $M_m$ , would have yielded a positive value and could have potentially been greater than that of a truly optimal design. Because we had two passbands that needed to be optimized, the metric,  $M_m$ , was maximized to obtain the optimal result. When running the optimization routine, multiplying the two  $F_i$  by each other ensures that both passbands have high transmission between the absorption edges and low transmission elsewhere. A secondary metric was used to confirm the usefulness of the design for a high magnitude  $M_m$ :

$$M_a = F_1 + F_2 \quad (3.3)$$

This metric,  $M_a$ , was unreliable in some cases, specifically those in which there was one very good and one very poor passband. It was much easier to see an ideal design with  $M_m$ , but  $M_a$  was useful to confirm the result. An optimized result will have very high values of both  $M_m$  and  $M_a$ .

### 3.4 Theoretically Optimal Design

Upon implementation of our optimization routine, we found the theoretically ideal design:

1st Filter: 1.8 $\mu\text{m}$  Zr with 0.2 $\mu\text{m}$  Be

2nd Filter: 6.8 $\mu\text{m}$  Al with 31.2 $\mu\text{m}$  Be

3rd Filter: 5.44 $\mu\text{m}$  Si with 28.56 $\mu\text{m}$  Be

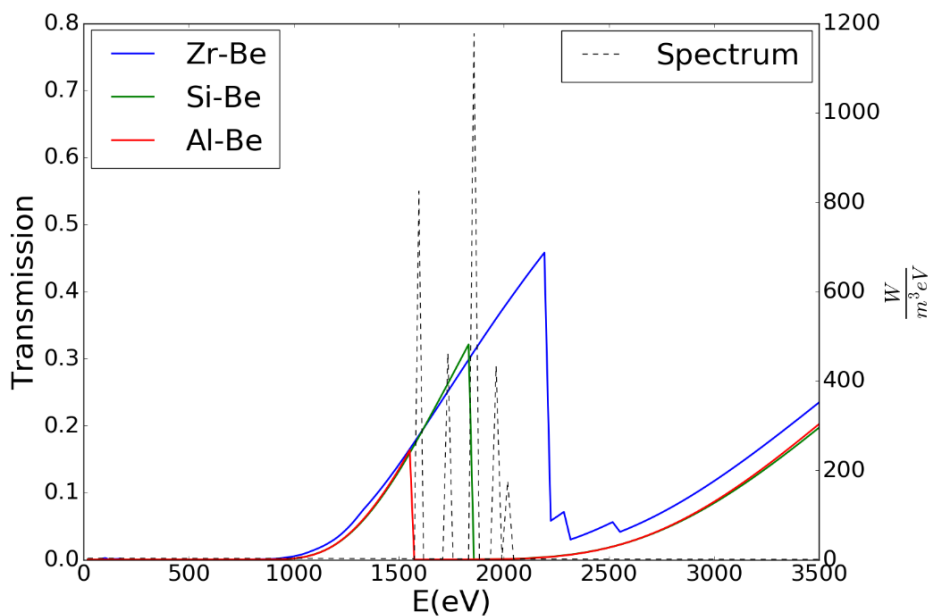


Figure 3.8: Plot of single filter transmission curves with a simulated x-ray spectrum. Total filter thicknesses were allowed to vary. Thickness of all six elements were allowed to vary to produce the theoretical optimum. Filter design: 1.8 $\mu\text{m}$  Zr with 0.2 $\mu\text{m}$  Be, 6.8 $\mu\text{m}$  Al with 31.2 $\mu\text{m}$  Be, and 5.44 $\mu\text{m}$  Si with 28.56 $\mu\text{m}$  Be

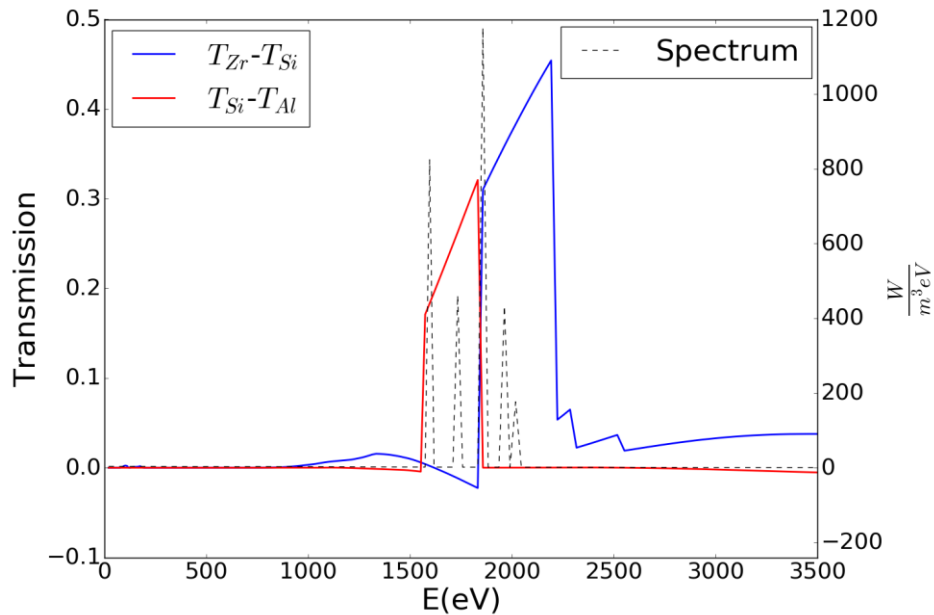


Figure 3.9: Plot of transmission curves of the passbands with a simulated x-ray spectrum. The two passbands are  $T_{Zr-T_{Si}}$  (Blue) and  $T_{Si-T_{Al}}$  (Red). Filter design:  $1.8\mu\text{m}$  Zr with  $0.2\mu\text{m}$  Be,  $6.8\mu\text{m}$  Al with  $31.2\mu\text{m}$  Be, and  $5.44\mu\text{m}$  Si with  $28.56\mu\text{m}$  Be

This result occurred before we employed the manufacturing restrictions. It served as a method of comparison for the final design. When comparing Figure 3.9 to that of 3.6, there is one noteworthy difference, the reduction in transmission of the  $T_{Zr-T_{Si}}$  passband within that of the  $T_{Si-T_{Al}}$  passband. This is the most important quality accounted for in our figure of merit due to the figure of merit being weighted against the spectrum and the immense brightness of the lines. Reducing the transmission of the  $T_{Zr-T_{Si}}$  passband within the other passband by even a seemingly negligible amount had a significant impact on improving the goal of separating the Al charge states. Two less noteworthy but still important changes are the reduced maximum transmission of the passbands and at energies greater than each passband. The reduced maximum transmission within the passband is not very important because of the massive brightness of the line radiation.

### 3.5 Final Design

Due to the inability to obtain 5  $\mu\text{m}$  Si wafers, we had to adjust our design for the real world. Implementing manufacturing limitations, we determined our final, realizable design was:

1st Filter: 1.8 $\mu\text{m}$  Zr with 0.2 $\mu\text{m}$  Be

2nd Filter: 6.8 $\mu\text{m}$  Al with 31.2 $\mu\text{m}$  Be

3rd Filter: 10.0 $\mu\text{m}$  Si with 12.7 $\mu\text{m}$  Be

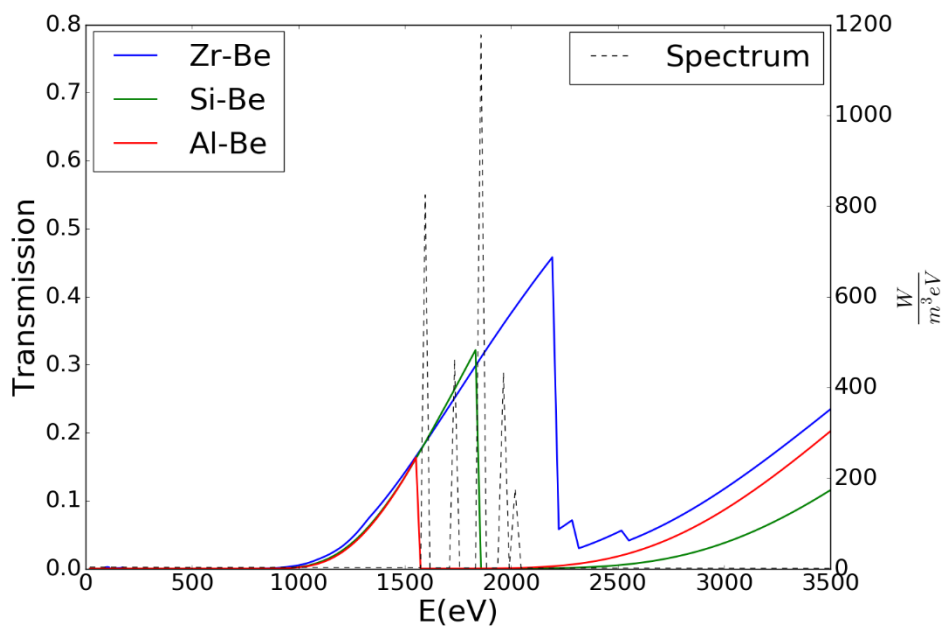


Figure 3.10: Plot of single filter transmission curves with a simulated x-ray spectrum. Thickness of all elements except Si were allowed to vary to produce the theoretical optimum. Filter design: 1.8 $\mu\text{m}$  Zr with 0.2 $\mu\text{m}$  Be, 6.8 $\mu\text{m}$  Al with 31.2 $\mu\text{m}$  Be, and 10.0 $\mu\text{m}$  Si with 12.7 $\mu\text{m}$  Be

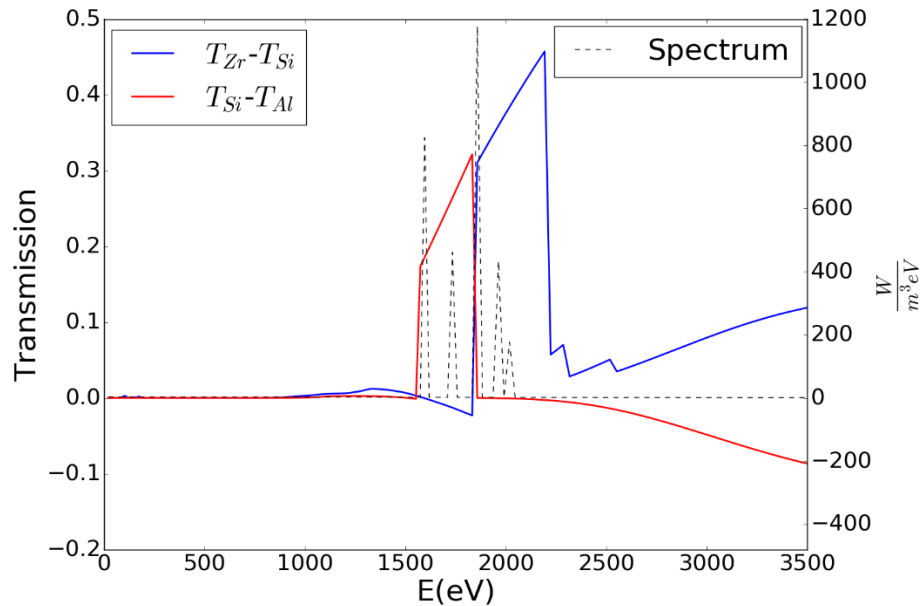


Figure 3.11: Plot of transmission of the passbands vs  $E(\text{eV})$  with a simulated x-ray spectrum for the physically realizable design. Filter design:  $1.8\mu\text{m}$  Zr with  $0.2\mu\text{m}$  Be,  $6.8\mu\text{m}$  Al with  $31.2\mu\text{m}$  Be, and  $10.0\mu\text{m}$  Si with  $12.7\mu\text{m}$  Be

The final filter design is similar to that of our theoretically optimal design. Only our 3<sup>rd</sup> filter, the Si filter, was changed. As a result, when compared to the optimal design [Figure 3.9], the final design [Figure 3.11] had worsened slightly. The Al and Zr filters were chosen to be unchanged to maintain high transmission. Maintaining higher transmission within the passband results in greater signal and a wider range of plasma parameters that the detector can take reliable measurements at. The only notable consequence of this is that the transmission of both passbands at  $E > 2223\text{eV}$  had clearly increased.

Due to our design having three detectors, there are three ways to subtract the signals. Even though attention was focused on the  $T_{\text{Zr}}-T_{\text{Si}}$  and  $T_{\text{Si}}-T_{\text{Al}}$  passbands, our third passband,  $T_{\text{Zr}}-T_{\text{Al}}$ , is also useful. Knowing that the filters of this third passband, Zr and Al, are components of the optimal design (i.e. only the Si filter changed), we expect this passband to still be optimized [Figure 3.12].

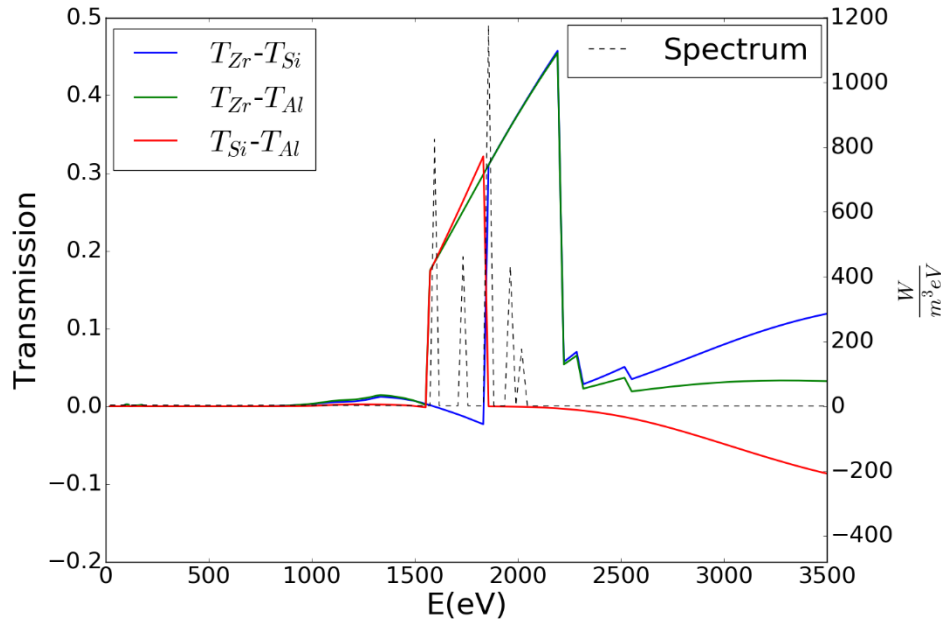


Figure 3.12: Plot of transmission of the passbands vs  $E(\text{eV})$  with a simulated x-ray spectrum for the physically realizable design. Filter design:  $1.8\mu\text{m}$  Zr with  $0.2\mu\text{m}$  Be,  $6.8\mu\text{m}$  Al with  $31.2\mu\text{m}$  Be, and  $10.0\mu\text{m}$  Si with  $12.7\mu\text{m}$  Be. All three possible passbands were plotted.

As expected, the passband is great. Obviously, using the  $T_{\text{Zr}}-T_{\text{Si}}$  and  $T_{\text{Si}}-T_{\text{Al}}$  passbands would be significantly worse than using the  $T_{\text{Zr}}-T_{\text{Al}}$  passband when measuring total Al line radiation signal. The transmission of the  $T_{\text{Zr}}-T_{\text{Al}}$  passband at  $E < 1559.6\text{eV}$  is virtually unchanged [Figure 3.12]. Secondly, the transmission of the  $T_{\text{Zr}}-T_{\text{Al}}$  passband at  $E > 2223\text{eV}$  is significantly lower than  $|T_{\text{Zr}}-T_{\text{Si}}| + |T_{\text{Si}}-T_{\text{Al}}|$ . Even though the continuum is rather small in this region compared to the Al lines, this transmission difference will have a noticeable impact in separating the total line radiation from the continuum. Secondly, there is no longer a transmission overlap from the  $T_{\text{Zr}}-T_{\text{Si}}$  passband within the  $T_{\text{Si}}-T_{\text{Al}}$  passband. Essentially, we are no longer measuring the same lines twice at different transmissions, improving the accuracy of NICKAL2. Obviously, this passband cannot be used for the intended purpose of separating  $\text{Al}^{11+}$  and  $\text{Al}^{12+}$  lines using the  $T_{\text{Zr}}-T_{\text{Si}}$  and  $T_{\text{Si}}-T_{\text{Al}}$  passbands, but it is the most effective method for measuring the total, unseparated Al line radiation.

The filters were manufactured by Lebow Inc. [Figure 3.13]. The filters have a  $\pm 10\%$  uncertainty in thickness [16]. This was the lowest uncertainty available for our filters. Moving away from transmission analysis, the best way to quantify the effectiveness of our final design with respect to its goals was through analyzing the signal. Through simulating the actual measurements, we sought to test whether: the vast majority of signal measured in the passbands is from Al lines; NICKAL2 accurately measures the total Al line radiation; and NICKAL2 separates the lines of each charge state.

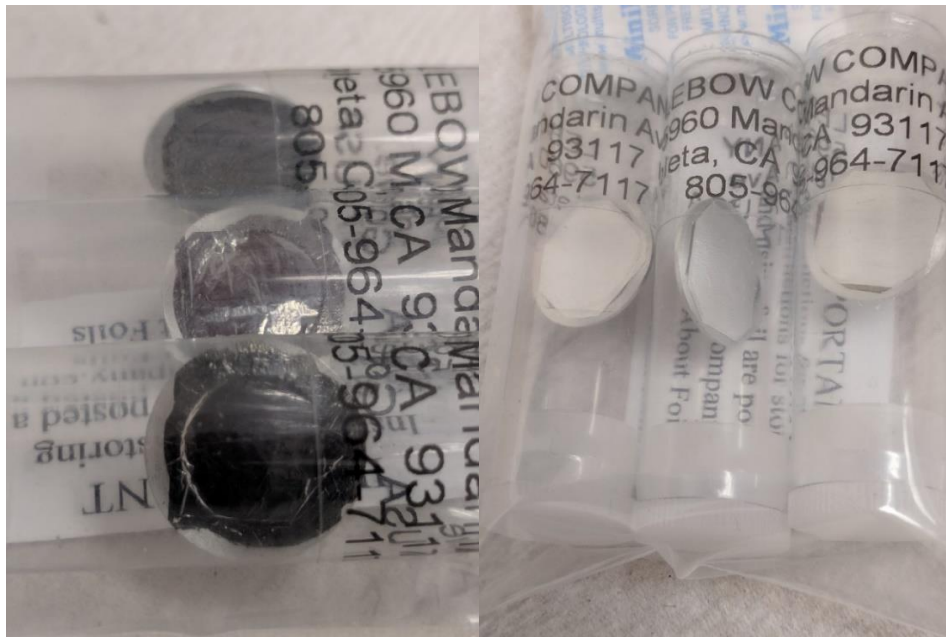


Figure 3.13 (a) (Left):  $1.8\mu\text{m Zr}-0.2\mu\text{m Be}$  filters with aluminum mounts. Filters were kept in bags for pictures due to their fragility. The filter mounted surface will be placed closest to the diode for assembly.

Figure 3.13 (b) (Right):  $6.8\mu\text{m Al}-31.2\mu\text{mBe}$  filters with aluminum mounts.



Figure 3.13 (c): 10.0 $\mu$ m Si-12.7 $\mu$ m Be filters with aluminum mounts

## Chapter 4

### Simulated Signal Analysis

Simulating MST plasmas and analyzing the signal using our final filter design was the next step in confirming the effectiveness of NICKAL2. Our main concern when performing this analysis was whether our initial assumption holds that the vast majority of the signal of each passband originates from Al line radiation. As a result, there were two parameters of interest that influence Al line radiation brightness significantly,  $n_e$  and  $T_e$ , so the dependence of the signal on the values at the core were analyzed for these two variables. PFM accounts for the local temperature and electron density values by calculating each respective profile [Figures 4.1 and 4.2]. These are the electron temperature and density profiles used for the following signal analyses. Even though the core values change, the shape of the electron temperature and density profiles are consistent for all of our simulated plasmas.

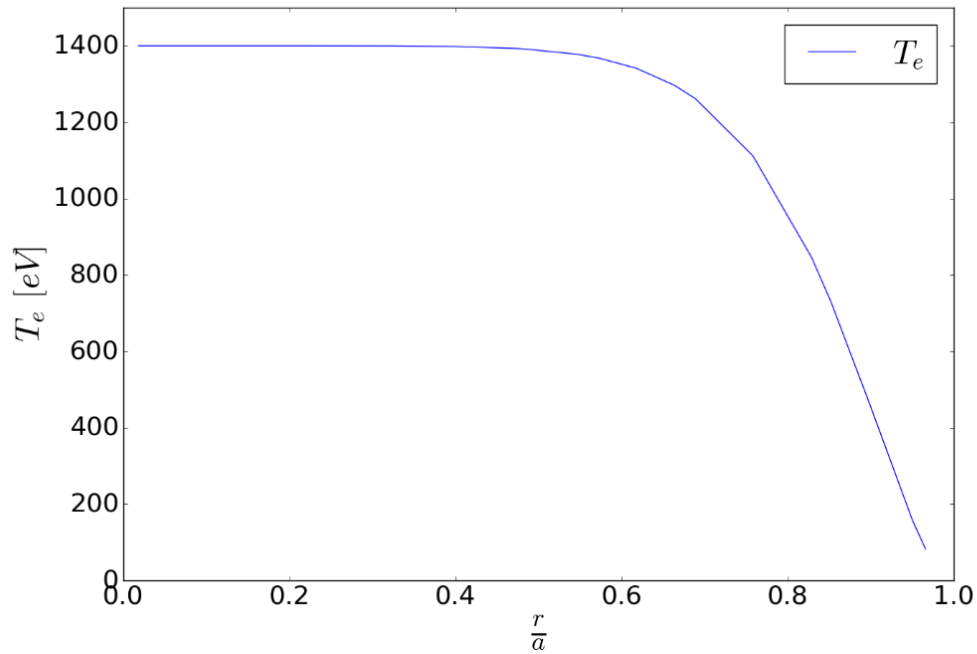


Figure 4.1: Example simulated electron temperature profiles. Plasma parameters:  $T_e(0)=1400\text{eV}$ ,  $n_e(0)=1.13\times 10^{19}\text{ m}^{-3}$ , and  $n_{Al}(0)=0.00108\times 10^{19}\text{ m}^{-3}$ , where  $T_e(0)$  and  $n_e(0)$  are respectively the electron temperature and density values at the core where the minor radius is zero.

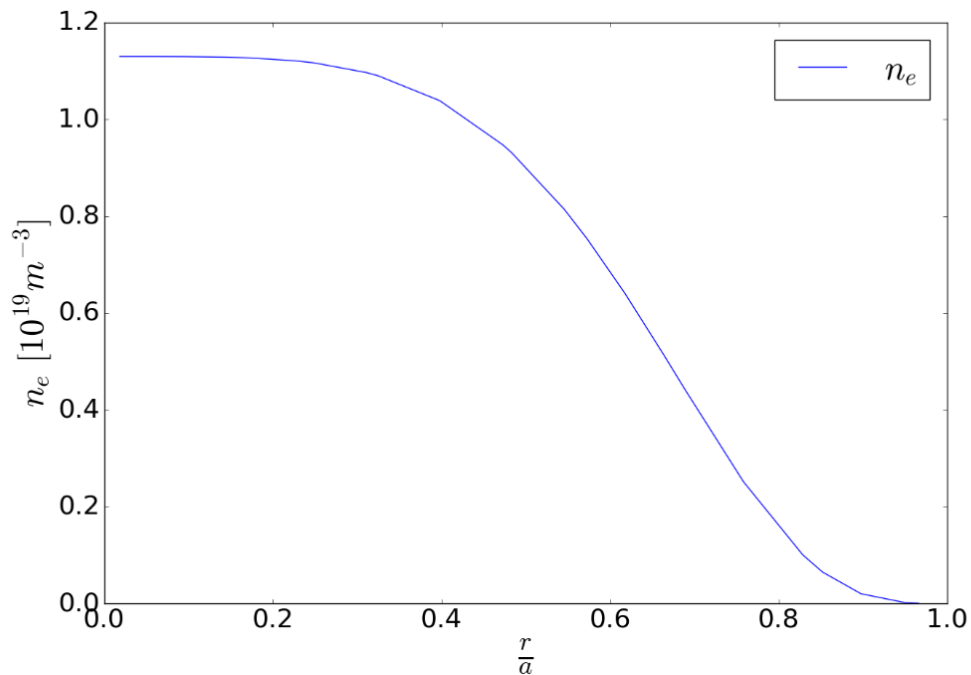


Figure 4.2: Example simulated electron density profile. Plasma parameters:  $T_e(0)=1400\text{eV}$ ,  $n_e(0)=1.13\times 10^{19}\text{ m}^{-3}$ , and  $n_{Al}(0)=0.00108\times 10^{19}\text{ m}^{-3}$ .

First, attention is focused on  $n_e$  followed by a similar analysis for  $T_e$ . In addition, by varying these parameters, we can model the effective separation of charge states. These simulations serve as a basis for comparison to physical data taken once assembly and installation is completed. In order to simulate our passbands, we simulated the signal of each separate filter using PFM [Figure 4.3]. The difference is then taken between the signal of each filter to determine the corresponding signal within the passband. The noise modelled for each signal is  $\pm 4\%$ . This is the approximate noise for the absolute signal of the SXT system. The SXT system uses similar hardware as the NICKAL2 detector. Because of this and the uncertainty of the measurements made by NICKAL2 being experimentally undetermined, we have used the  $\pm 4\%$  for our simulations. The uncertainty remained the same for our passband simulations. Due to the passband signal not being the absolute signal (i.e. the signal from each filtered detector)  $\pm 4\%$  is a conservative estimate for the passbands.

#### 4.1 Al Line Radiation Dependence on $n_e$

For our simulations,  $0.1 \times 10^{19} \text{m}^{-3} \leq n_e(0) \leq 1.5 \times 10^{19} \text{m}^{-3}$ . This range encompasses the range of core  $n_e$  values, although most plasmas in MST have  $n_e(0) \geq 0.4 \times 10^{19} \text{m}^{-3}$ . The signal for each filter as a function of core  $n_e$  is shown in Figure 4.3. As expected, the signal is very high in the Zr and Si filters, while that of Al is near zero. This is because no Al lines are present before the K-edge of Al, so its signal is mostly from continuum radiation.

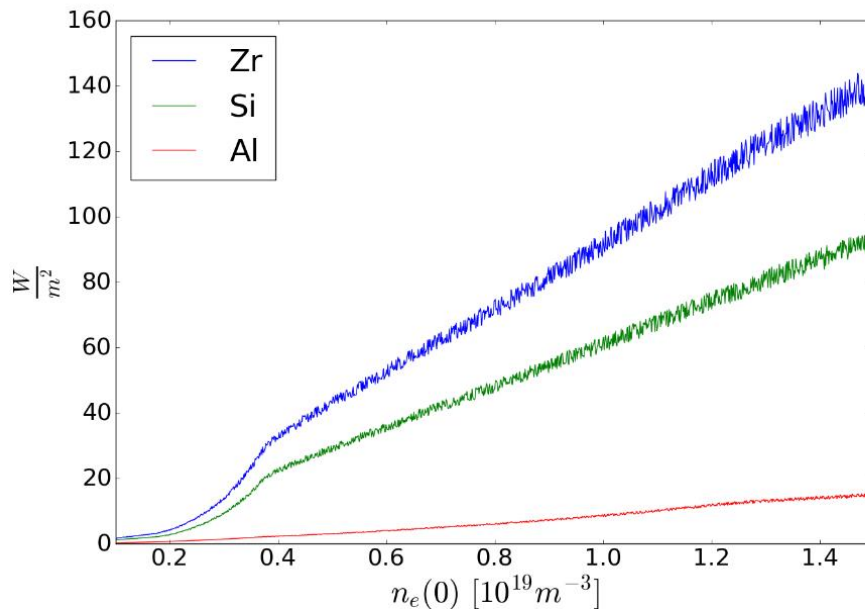


Figure 4.3: Simulated signal from each respective filter using the final filter design. parameters:  $T_e(0)=1400\text{eV}$ ,  $n_{\text{Al}}(0)=0.00108 \times 10^{19} \text{ m}^{-3}$ , where  $T_e(0)$  and  $n_e(0)$  are respectively the electron temperature and density values at the core where the minor radius is zero.

Utilizing these filters, we calculated the total signal of the passbands as a function of  $n_e(0)$  [Figure 4.4 and 4.5]. For measuring the total Al line radiation signal, the total signal of the  $T_{\text{Zr}}\text{-}T_{\text{Al}}$  passband determines the minimum  $n_e(0)$ , denoted  $n^{(1)}_{\text{min}}$ , at which we can accurately make measurements [Figure 4.5]. In general, we trust signal measurements of  $\geq 1 \text{ W/m}^2$ . As a result,  $n^{(1)}_{\text{min}} < 0.1 \times 10^{19} \text{ m}^{-3}$  when using the  $T_{\text{Zr}}\text{-}T_{\text{Al}}$  passband. This is significantly less than the core values typically seen within MST plasmas.

Similarly, we define  $n^{(2)}_{\text{min}}$  to be the minimum  $n_e(0)$  at which we could accurately measure signal from the partially separated  $\text{Al}^{11+}$  and  $\text{Al}^{12+}$  lines using the  $T_{\text{Zr}}\text{-}T_{\text{Si}}$  and  $T_{\text{Si}}\text{-}T_{\text{Al}}$  passband combination. This is determined by the passband that measures a signal of at least  $1 \text{ W/m}^2$  at the lowest  $n_e(0)$  without the signal ever going below  $1 \text{ W/m}^2$  at all higher  $n_e(0)$ . As can

be seen in Fig 4.5,  $n_{\min}^{(2)}$  is determined by the  $T_{Zr}-T_{Si}$  passband as expected, so  $n_{\min}^{(2)} \sim 0.10 \times 10^{19} \text{ m}^{-3}$ . As is the case for the  $T_{Zr}-T_{Al}$  passband,  $n_{\min}^{(2)} < 0.4 \times 10^{19} \text{ m}^{-3}$ .

Both  $n_{\min}^{(1)}$  and  $n_{\min}^{(2)}$  are determined using a simulated  $T_e(0)=1.4\text{keV}$  plasma. If  $T_e(0)$  is decreased, we expect lower overall signal and, therefore, higher  $n_{\min}^{(1)}$  and  $n_{\min}^{(2)}$ . It is unlikely that  $n_{\min}^{(1)}$  and  $n_{\min}^{(2)}$  would increase enough to be within  $0.4 \times 10^{19} \text{ m}^{-3} \leq n_e(0) \leq 1.5 \times 10^{19} \text{ m}^{-3}$ , therefore, it is unlikely that there is a lower limit on  $n_e(0)$  for the measurements using NICKAL2. Trusting signal measurements of  $\geq 1 \text{ W/m}^2$  is more of a lower limit on absolute signals, therefore, our estimate here, based on the signal in the passband, is fairly conservative. As a result, we can expect lower  $n_{\min}^{(1)}$  and  $n_{\min}^{(2)}$ , but even at lower  $n_{\min}^{(1)}$  and  $n_{\min}^{(2)}$ , we are already outside of the  $n_e(0)$  range of MST plasmas.  $n_{\min}^{(1)}$  and  $n_{\min}^{(2)}$  would improve, but it would not affect the application of NICKAL2 significantly because we would still have both  $n_{\min}^{(1)} \leq 0.4 \times 10^{19} \text{ m}^{-3}$  and  $n_{\min}^{(2)} \leq 0.4 \times 10^{19} \text{ m}^{-3}$ .

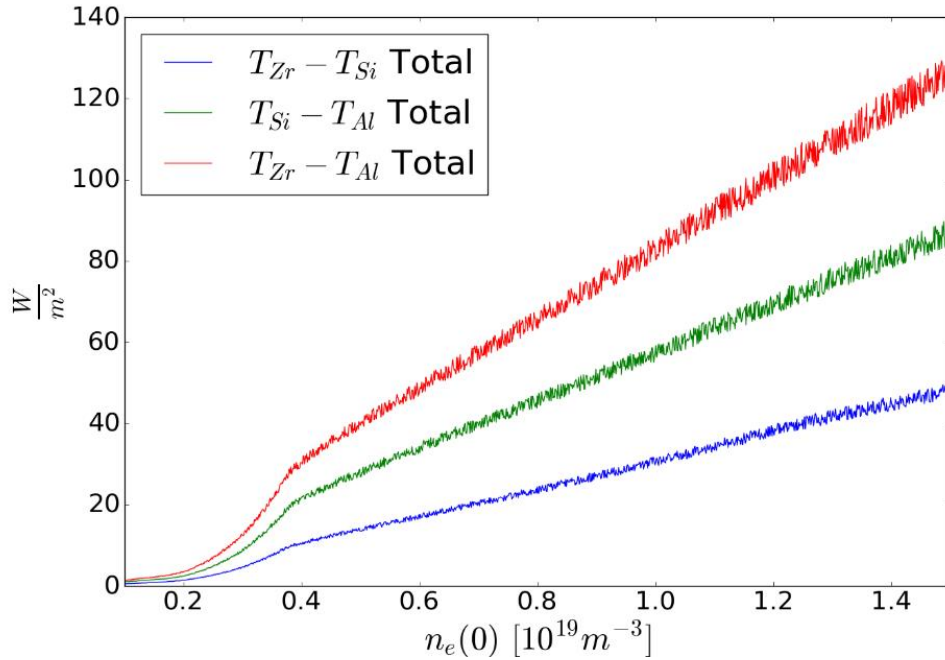


Figure 4.4: Simulated total signal from each respective passband using the final filter design. Plasma parameters:  $T_e(0)=1400\text{eV}$ ,  $n_{Al}(0)=0.00108 \times 10^{19} \text{ m}^{-3}$ .

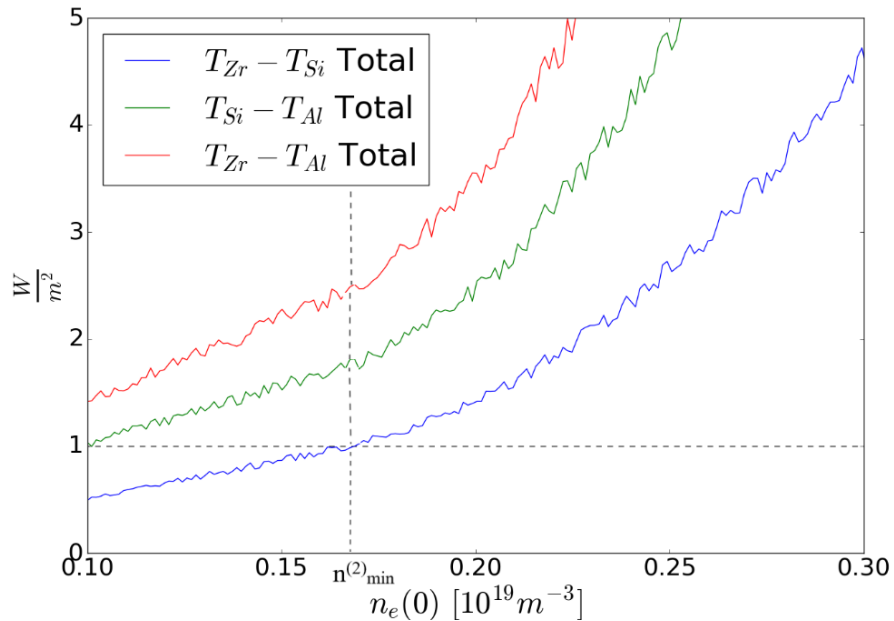


Figure 4.5: Zoom in of simulated signal from each respective passband using the final filter design. This is the same data as that of Figure 4.2. Plasma parameters:  $T_e(0)=1400\text{eV}$ ,  $n_{\text{Al}}(0)=0.00108 \times 10^{19} \text{ m}^{-3}$ .

Determining that  $n_e(0)$  should not strongly impact our measurement range in MST, we next considered whether our initial assumption, which was the signal being entirely that of Al lines, was correct. The signals of the passbands are separated out into each type of x-rays that make up the SXR spectrum [Figure 4.6, 4.7, and 4.8]. As can clearly be seen in Figs 4.7 and 4.8, the signal from both the  $T_{\text{Zr}}-T_{\text{Al}}$  and  $T_{\text{Si}}-T_{\text{Al}}$  passbands is virtually all line radiation. On the other hand, the signal from the  $T_{\text{Zr}}-T_{\text{Si}}$  passband signal is not. Line radiation does make up the majority of the signal, but accounting of the continuum must nevertheless be.

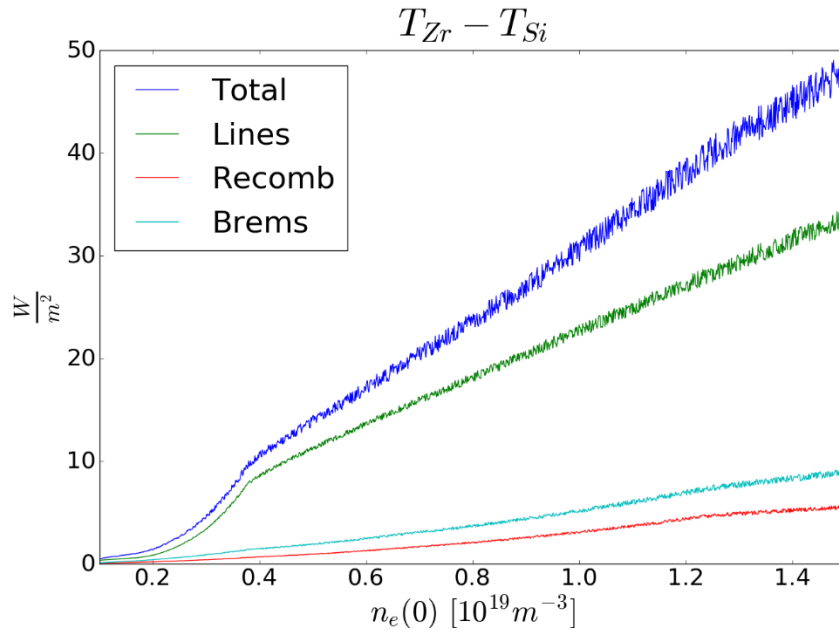


Figure 4.6: Simulated signal separated into the the signal from all SXR (blue), line (green), recombination (red), and bremsstrahlung (cyan) radiation for the  $T_{Zr}-T_{Si}$  passband as a function of  $n_e(0)$ . Plasma parameters:  $T_e(0)=1400\text{eV}$ ,  $n_{Al}(0)=0.00108 \times 10^{19} m^{-3}$ .

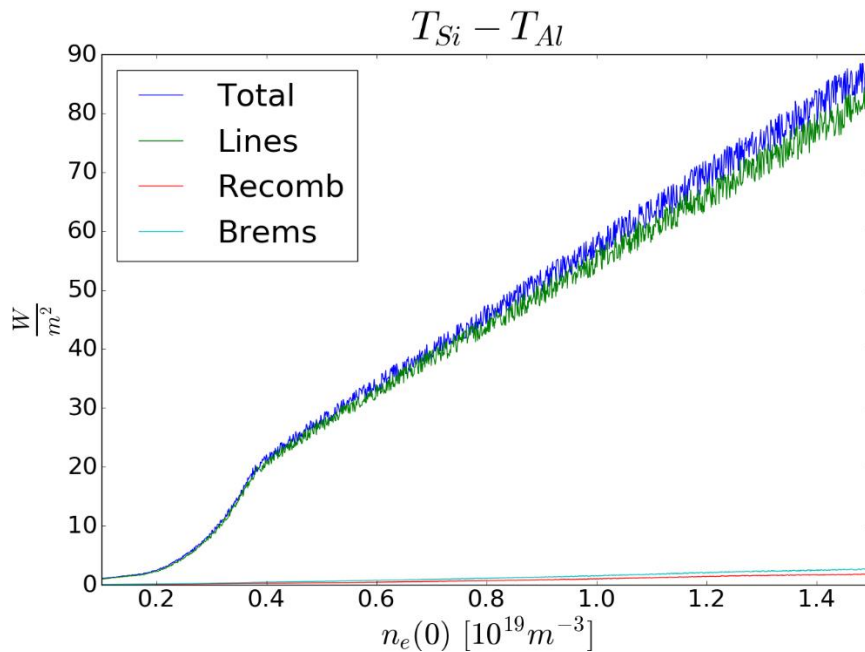


Figure 4.7: Simulated signal separated into the the signal from all SXR (blue), line (green), recombination (red), and bremsstrahlung (cyan) radiation for the  $T_{Si}-T_{Al}$  passband as a function of  $n_e(0)$ . Plasma parameters:  $T_e(0)=1400\text{eV}$ ,  $n_{Al}(0)=0.00108 \times 10^{19} m^{-3}$ .

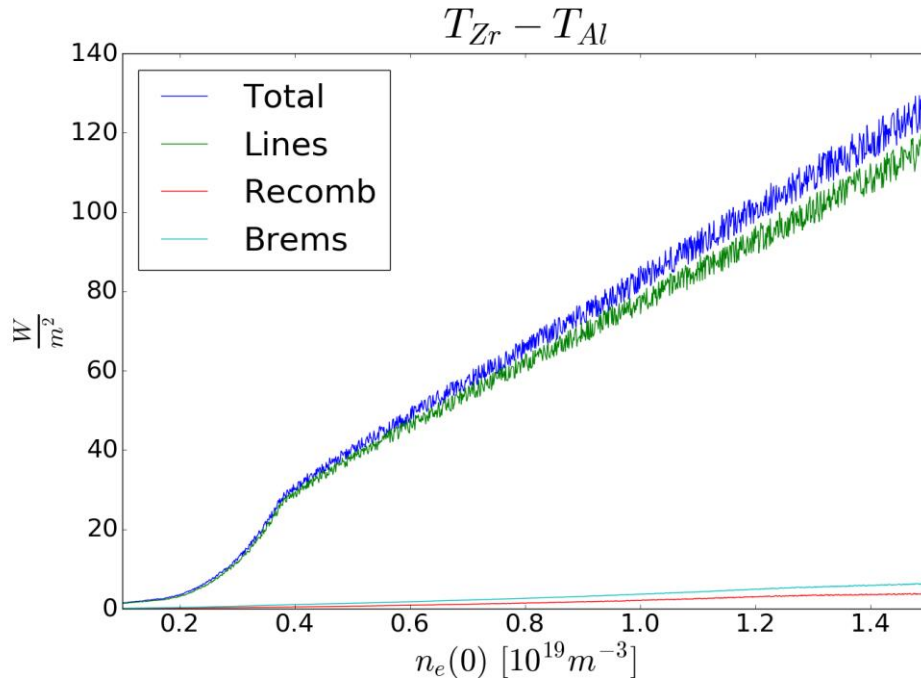


Figure 4.8: Simulated signal separated into the the signal from all SXR (blue), line (green), recombination (red), and bremsstrahlung (cyan) radiation for the  $T_{Zr}-T_{Al}$  passband as a function of  $n_e(0)$ . Plasma parameters:  $T_e(0)=1400\text{eV}$ ,  $n_{Al}(0)=0.00108 \times 10^{19} \text{ m}^{-3}$ .

An easier way to see the domination of line radiation is through calculating the ratio of the line radiation signal to the total signal [Figure 4.9]. This proves that our measurements should be virtually all line radiation signal for the  $T_{Zr}-T_{Al}$  and  $T_{Si}-T_{Al}$  passband at all realistic  $n_e(0)$  for MST. The ratios of line radiation signal to the total signal for these two passbands are always larger than 0.85 when considering the noise. Even though the contribution from line radiation to the  $T_{Zr}-T_{Si}$  signal is not as large as we would have liked, it is sufficient at  $n_e(0) \geq 0.4 \times 10^{19} \text{ m}^{-3}$ .  $T_{Zr}-T_{Si}$  passband mainly serves the purpose of separating as much of the  $Al^{12+}$  lines from the  $T_{Si}-T_{Al}$  passband as possible. In addition, the ratio is virtually constant at  $n_e(0) \geq 0.4 \times 10^{19} \text{ m}^{-3}$  for all passbands, signifying that the relative brightness of lines does not vary significantly with density for most MST relevant densities.

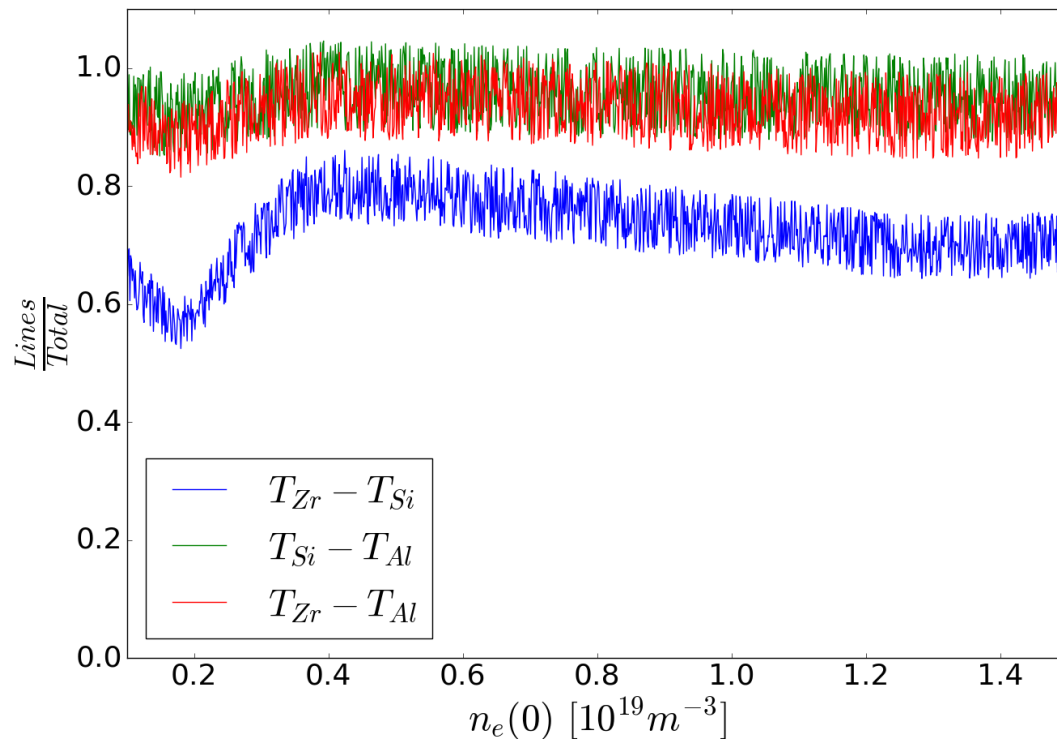


Figure 4.9: Simulated signal ratio of line radiation signal to the total signal for each passband. The uncertainties have been propagated. Plasma parameters:  $T_e(0)=1400\text{eV}$ ,  $n_{\text{Al}}(0)=0.00108 \times 10^{19} \text{ m}^{-3}$ .

To address the secondary goal of the detector, we looked at the ratio of  $\text{Al}^{11+}$  line radiation to  $\text{Al}^{12+}$  line radiation [Figure 4.10]. This is not an experimentally measurable quantity due to the inability of NICKAL2 to completely separate the  $\text{Al}^{11+}$  and  $\text{Al}^{12+}$  lines and the relatively significant continuum contribution to the signal of the  $T_{\text{Zr}}-T_{\text{Si}}$  passband.  $\text{Al}^{11+}$  lines dominate the  $\text{Al}^{12+}$  signal at  $n_e(0) \geq 0.4 \times 10^{19} \text{ m}^{-3}$ . Clearly, NICKAL2 cannot completely separate charge states at  $T_e(0)=1400\text{eV}$  for all  $n_e(0)$ . An important feature of Figure 4.10 is the constant ratio. The constant ratio signifies that the ratio of the signals from the charge states and line emissivity is independent of  $n_e(0)$  at  $n_e(0) \geq 0.4 \times 10^{19} \text{ m}^{-3}$ .

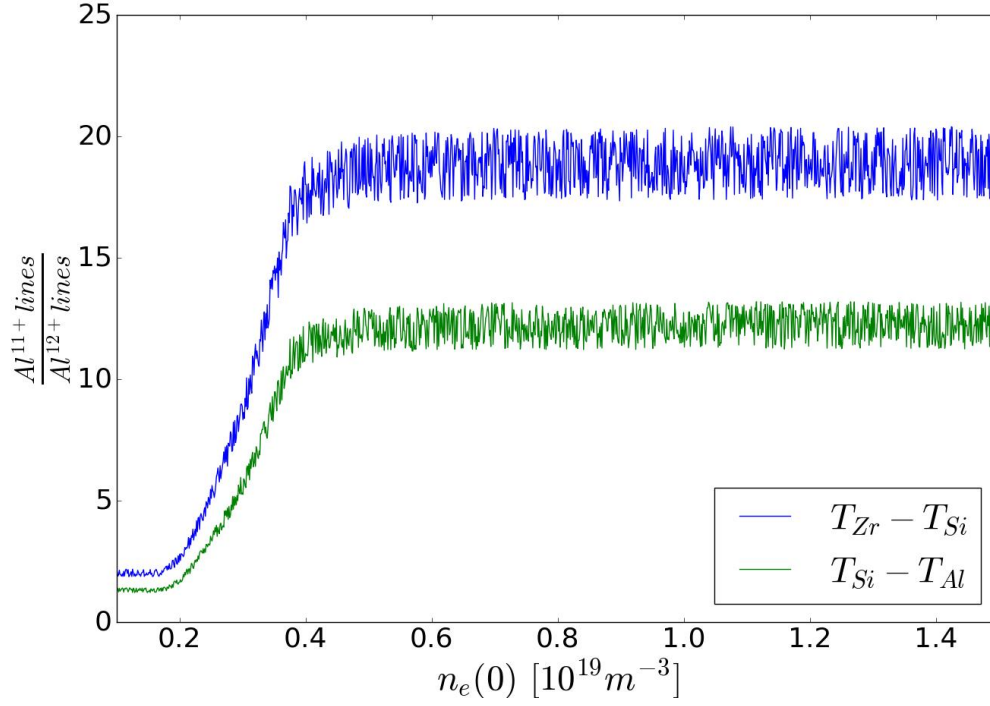


Figure 4.10: Simulated signal ratio of  $Al^{11+}$  line radiation signal to the  $Al^{12+}$  line radiation signal for the  $T_{Zr}-T_{Si}$  and  $T_{Si}-T_{Al}$  passband. The uncertainties have been propagated. Plasma parameters:  $T_e(0)=1400\text{eV}$ ,  $n_{Al}(0)=0.00108\times 10^{19}\text{ m}^{-3}$ .

Through analyzing the signals dependence on  $n_e(0)$ , we have determined an estimated measurement range for NICKAL2. When using at least one passband, our measurement ranges have the lower bound of the lowest value  $n_{\min}$ . This is determined depending on which filter is used in the passband(s) for the measurement. When measuring the total Al line radiation and incorporating this into the SXT analysis, the lower bound is determined by  $T_{Zr}-T_{Al}$ , so  $n_{\min}^{(1)} < 0.1 \times 10^{19} \text{ m}^{-3}$ . For partially separating the charge states using the designated passbands,  $n_{\min}^{(2)} \sim 0.17 \times 10^{19} \text{ m}^{-3}$  as determined by the  $T_{Zr}-T_{Si}$  passband.

## 4.2 Al Line Radiation Dependence on $T_e$

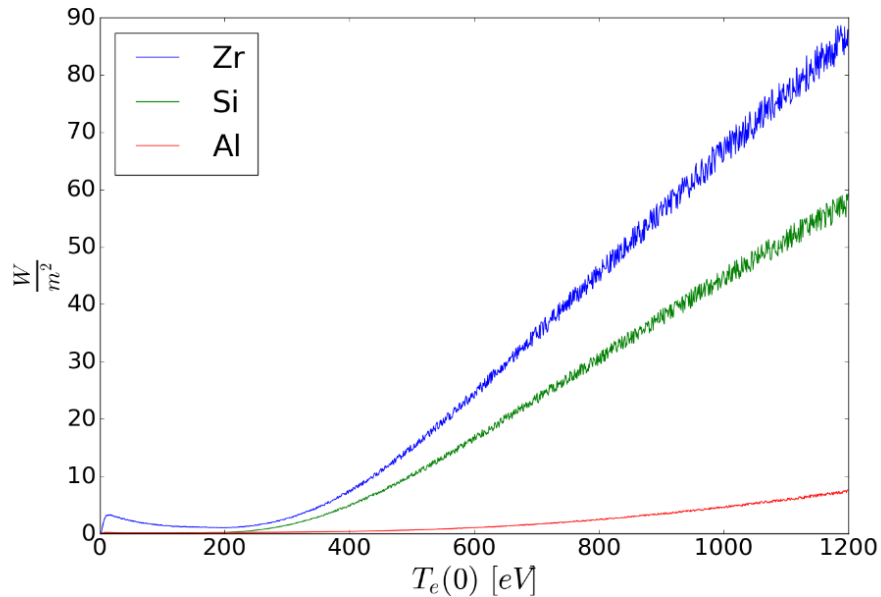


Figure 4.11: Simulated signal from each respective filter using the final filter design. Plasma parameters:  $n_e(0)=1.13 \times 10^{19} \text{ m}^{-3}$ ,  $n_{\text{Al}}(0)=0.00108 \times 10^{19} \text{ m}^{-3}$ .

As mentioned previously, the brightness of the Al lines also depends on  $T_e$ . Analogous to that which was done for analysis when varying  $n_e(0)$ , we simulated the signal of an MST plasma for each filter as a function of  $T_e(0)$  [Figure 4.11] and the signal from each passband [Figures 4.12 and 4.13]. For measuring the total Al line radiation signal, the total signal of the  $T_{\text{Zr}}\text{-}T_{\text{Al}}$  passband determined the minimum  $T_e(0)$ , denoted  $T_{\text{min}}^{(1)}$ , at which we could accurately make measurements [Figure 4.13]. As mentioned previously, we trust signal measurements of  $\geq 1 \text{ W/m}^2$ . As a result,  $T_{\text{min}}^{(1)} \sim 225 \text{ eV}$  when using the  $T_{\text{Zr}}\text{-}T_{\text{Al}}$  passband. Combining the measurements made by NICKAL2 with those made by the SXT system means we can likely extend the SXT temperature range to  $T_e \geq 225 \text{ eV}$ . This is a significant improvement over the current range of  $T_e \geq 1 \text{ keV}$ .

Similarly, we define  $T_{\text{min}}^{(2)}$  to be the minimum  $T_e(0)$  at which we could accurately measure signal from the partially separated  $\text{Al}^{11+}$  and  $\text{Al}^{12+}$  lines using the  $T_{\text{Zr}}\text{-}T_{\text{Si}}$  and  $T_{\text{Si}}\text{-}T_{\text{Al}}$

passbands. This is determined by the passband that measures a signal of at least  $1 \text{ W/m}^2$  at the lowest  $T_e(0)$  without the signal ever going below  $1 \text{ W/m}^2$  at all higher  $T_e(0)$ . As can be seen in Fig 4.3,  $T_{\min}^{(2)}$  is determined by the  $T_{Zr}-T_{Si}$  passband as expected, so  $T_{\min}^{(2)} \sim 275 \text{ eV}$ .

Both  $T_{\min}^{(1)}$  and  $T_{\min}^{(2)}$  are determined using a simulated  $n_e(0) = 1.13 \times 10^{19} \text{ m}^{-3}$  plasma. If  $n_e(0)$  is decreased, we expect lower overall signal and, therefore, higher  $T_{\min}^{(1)}$  and  $T_{\min}^{(2)}$ . As mentioned before, trusting signal measurements of  $\geq 1 \text{ W/m}^2$  is more of a lower limit on absolute signals, therefore, our estimate is fairly conservative. As a result, we can expect lower  $T_{\min}^{(1)}$  and  $T_{\min}^{(2)}$ . Due to the signal of the  $T_{Zr}-T_{Al}$  passband being greater than  $\sim 0.8 \text{ W/m}^2$  at virtually all  $T_e > 0$  [Figure 4.13], the lower signal limit could potentially lower  $T_{\min}^{(1)}$  to  $T_{\min}^{(1)} \sim 0 \text{ eV}$ , virtually eliminating the lower limit of the measurement range of the SXT system. In addition, the lower signal limit should decrease  $T_{\min}^{(2)}$  some, but not nearly to the extent that  $T_{\min}^{(2)}$  would be decreased. This is due to the very low signal of the  $T_{Si}-T_{Al}$  passband at  $T_e < 200 \text{ eV}$ .

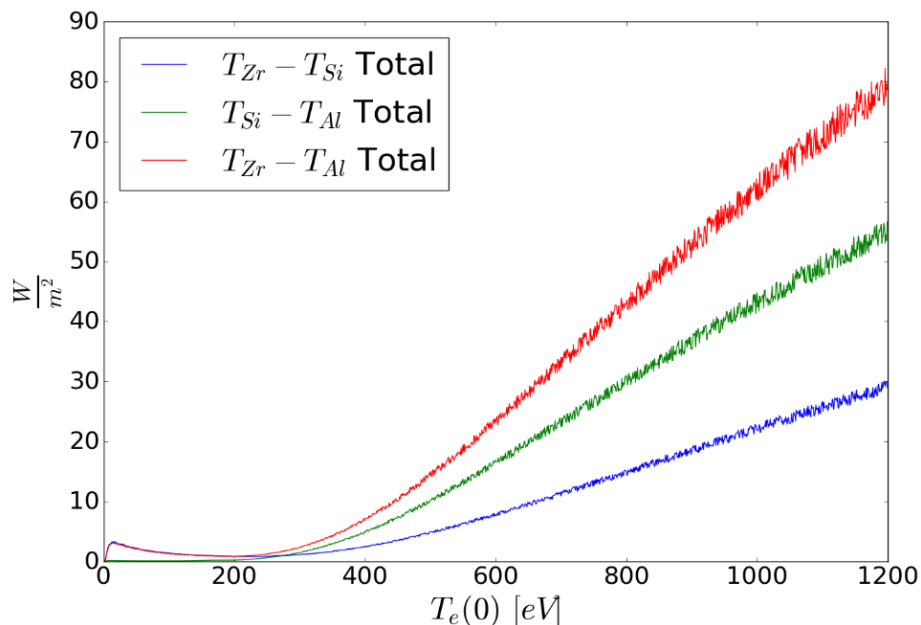


Figure 4.12: Simulated total signal from each respective passband using the final filter design. Plasma parameters:  $n_e(0) = 1.13 \times 10^{19} \text{ m}^{-3}$ ,  $n_{Al}(0) = 0.00108 \times 10^{19} \text{ m}^{-3}$ .

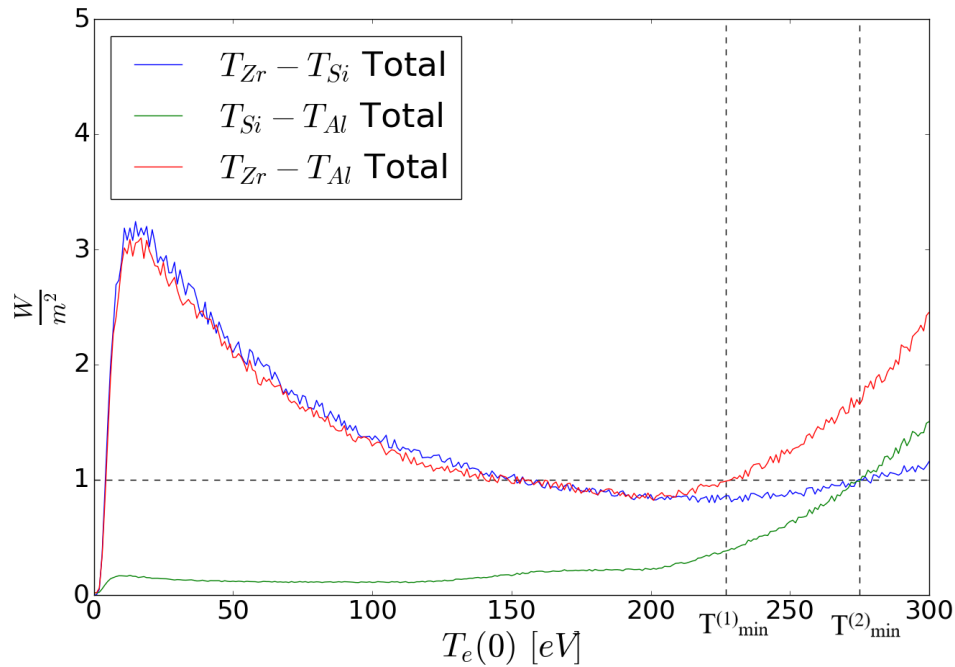


Figure 4.13: Simulated total signal from each respective passband using the final filter design. This is the same data as that of Figure 4.2. Plasma parameters:  $n_e(0)=1.13 \times 10^{19} \text{ m}^{-3}$ ,  $n_{Al}(0)=0.00108 \times 10^{19} \text{ m}^{-3}$ .

In order to have high confidence in this conclusion based on simulation, we wanted to check that the signal from the  $T_{Zr}-T_{Al}$  passband is mostly line radiation, or under what conditions that could be true. Looking at Figures 4.14, 4.15, and 4.16, we determined that the signal from the  $T_{Zr}-T_{Al}$  and  $T_{Si}-T_{Al}$  passbands are virtually all Al lines, which is consistent with the previous analysis varying  $n_e(0)$ . This gives us confidence that we can use the NICKAL2 detector to increase the range of measurement for the SXT system. Looking at the separated SXR sources of the signal of each passband [Figures 4.15 and 4.16], we determined that the  $T_{Zr}-T_{Al}$  signal are virtually all lines. Again, the  $T_{Zr}-T_{Si}$  passband is a concern [Figure 4.14]. The majority of signal was still from line radiation, but the relative contribution is lower than we would have liked.

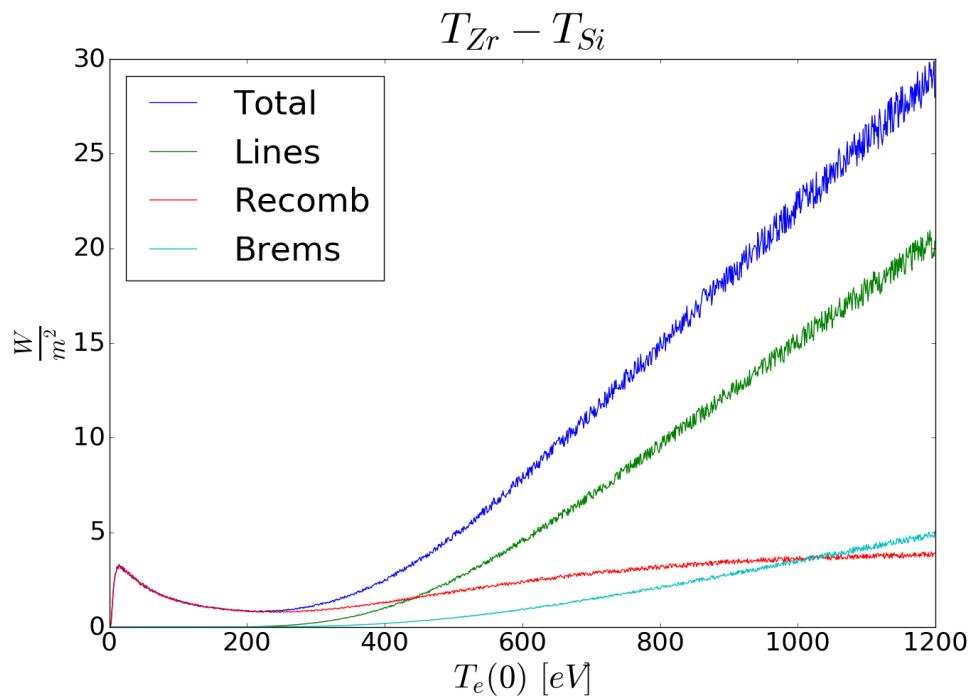


Figure 4.14: Simulated signal separated into the the signal from all SXR (blue), line (green), recombination (red), and bremsstrahlung (cyan) radiation for the  $T_{Zr}-T_{Si}$  passband as a function of  $T_e(0)$ . Plasma parameters:  $n_e(0)=1.13 \times 10^{19} \text{ m}^{-3}$ ,  $n_{Al}(0)=0.00108 \times 10^{19} \text{ m}^{-3}$ .

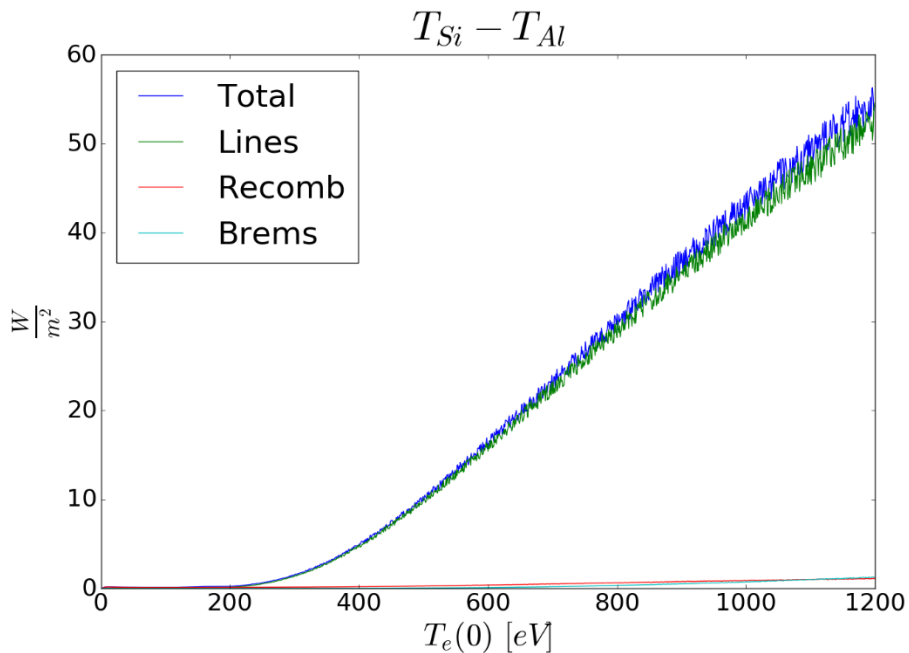


Figure 4.15: Simulated signal separated into the the signal from all SXR (blue), line (green), recombination (red), and bremsstrahlung (cyan) radiation for the  $T_{Si}-T_{Al}$  passband as a function of  $T_e(0)$ . Plasma parameters:  $n_e(0)=1.13 \times 10^{19} \text{ m}^{-3}$ ,  $n_{Al}(0)=0.00108 \times 10^{19} \text{ m}^{-3}$ .

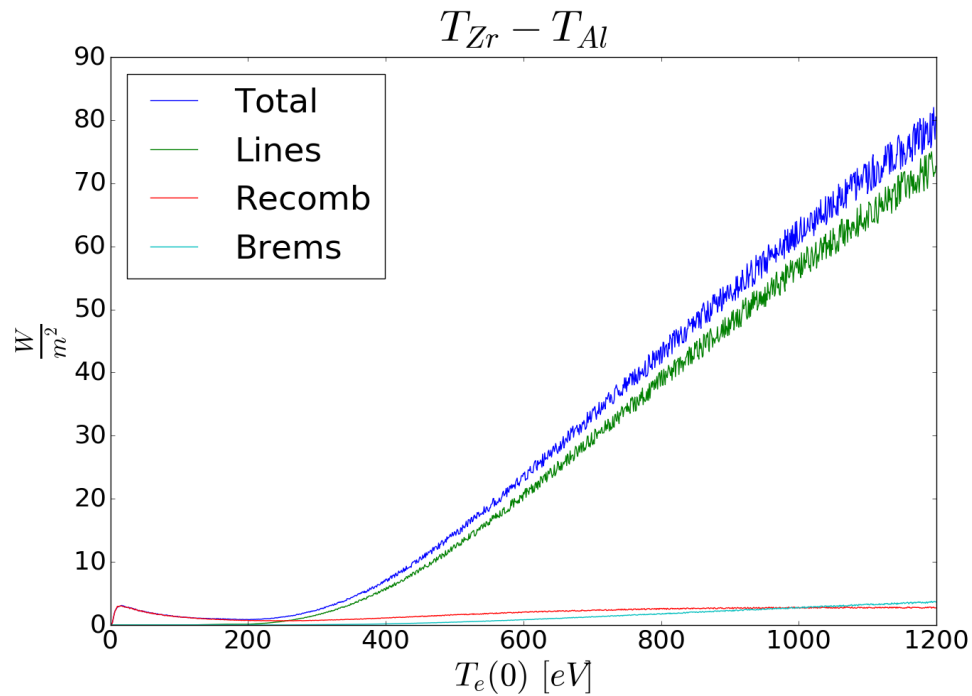


Figure 4.16: Simulated signal separated into the the signal from all SXR (blue), line (green), recombination (red), and bremsstrahlung (cyan) radiation for the  $T_{Zr}-T_{Al}$  passband as a function of  $T_e(0)$ . Plasma parameters:  $n_e(0)=1.13 \times 10^{19} \text{ m}^{-3}$ ,  $n_{Al}(0)=0.00108 \times 10^{19} \text{ m}^{-3}$ .

The ratio of lines to total signal helped reveal the usefulness of the  $T_{Zr}-T_{Si}$  passband [Figure 4.17]. We noticed that there is gradual increase in the ratio starting at  $T_e(0) \sim 150 \text{ eV}$ . The ratio of the  $T_{Si}-T_{Al}$  passband also rapidly increases at  $T_e(0) \sim 150 \text{ eV}$ . In addition, there is a slight plateau occurring at  $T_e(0) \sim 200 \text{ eV}$ . The rapid increase in the ratio of line radiation signal to total signal at  $T_e(0) \sim 150 \text{ eV}$  is likely due to the  $Al^{11+}$  charge state becoming populated. The plateau at  $T_e(0) \sim 200 \text{ eV}$  likely signifies Al atoms beginning to become ionized into the  $Al^{12+}$  charge state.

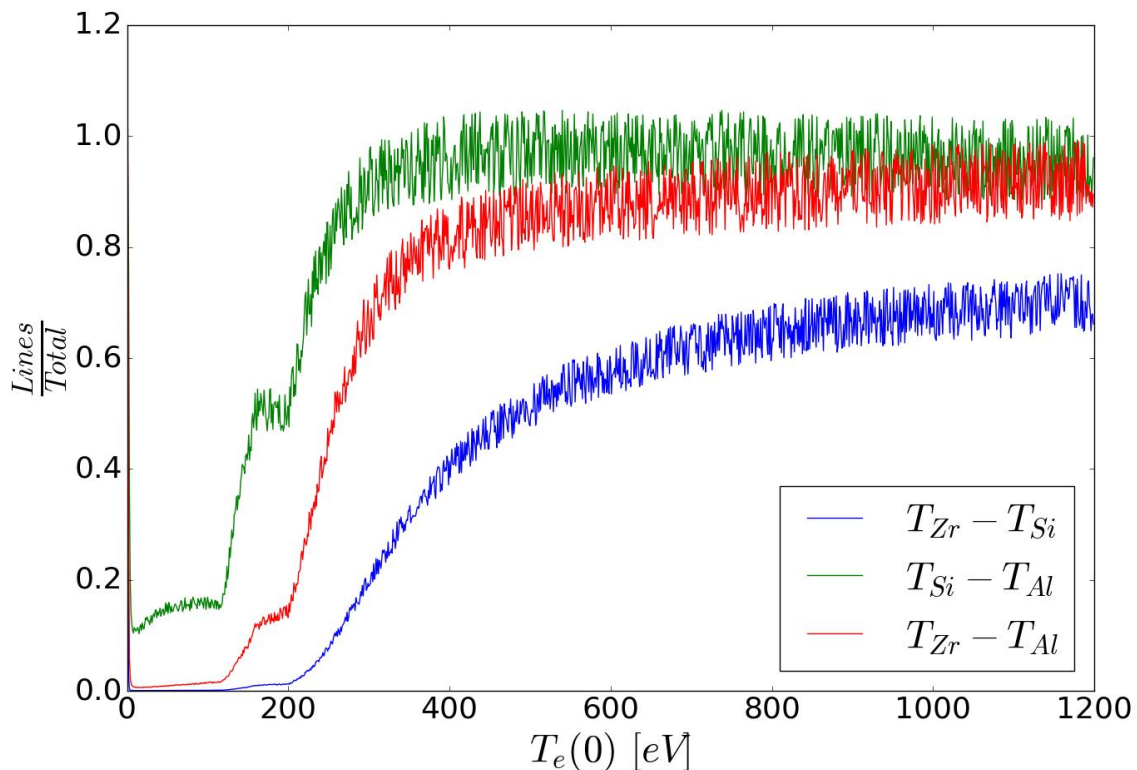


Figure 4.17: Simulated signal ratio of line radiation signal to the total signal for each passband. The uncertainties have been propagated. Plasma parameters:  $n_e(0)=1.13 \times 10^{19} \text{ m}^{-3}$ ,  $n_{Al}(0)=0.00108 \times 10^{19} \text{ m}^{-3}$ .

Again, looking at the ratio of  $Al^{11+}$  to  $Al^{12+}$  line radiation signal [Figure 4.18], both passbands are dominated by  $Al^{11+}$  lines. The increase in signal within the  $T_{Si}-T_{Al}$  passband due to the  $Al^{12+}$  lines is completely dwarfed by the new  $Al^{11+}$  lines. As a result, we conclude that we do not have the ability to completely separate charge states. Although this is expected, we do see a partial separation of charge states, particularly at low temperatures. Even though we are unable to measure  $Al^{12+}$  signal exclusively using NICKAL2, it may be possible to effectively determine the signal from each charge state with a combination of other MST diagnostics and computer simulations. The fact there is a maximum of one  $Al^{12+}$  and two  $Al^{11+}$  lines within the  $T_{Si}-T_{Al}$  passband may make it more probable to extrapolate the signal of each charge state within this passband.

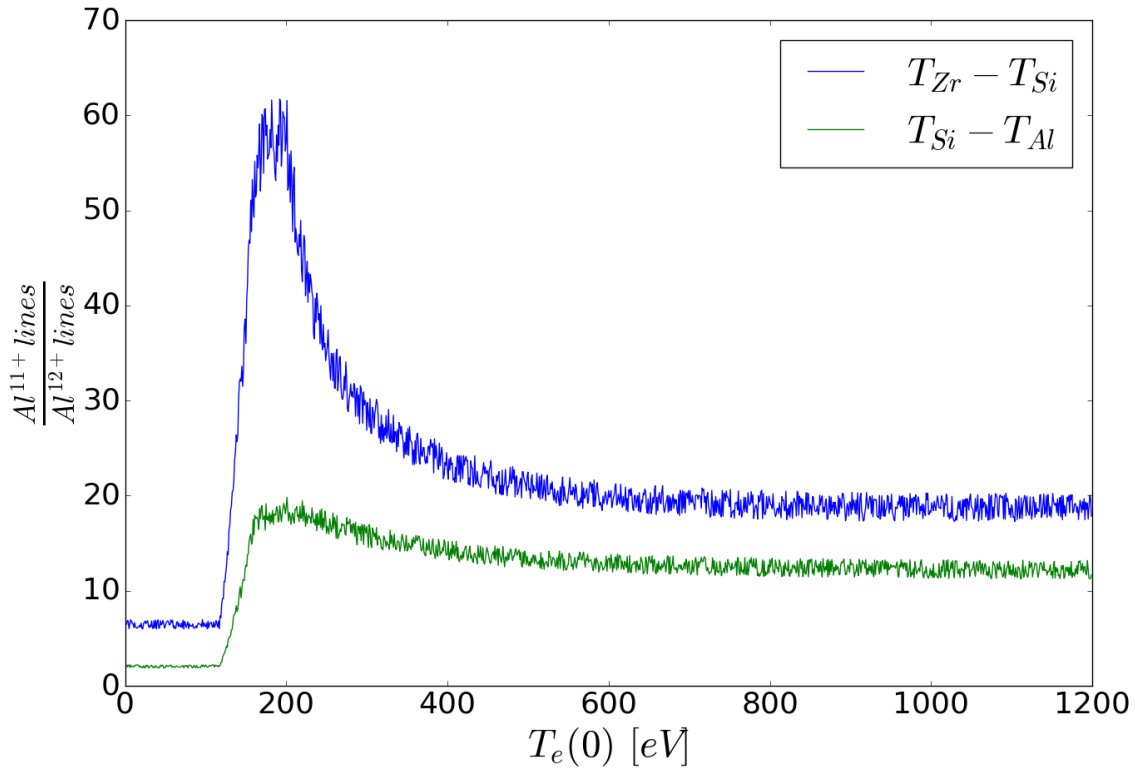


Figure 4.18: Simulated signal ratio of  $\text{Al}^{11+}$  line radiation signal to the  $\text{Al}^{12+}$  line radiation signal for the  $T_{Zr}-T_{Si}$  and  $T_{Si}-T_{Al}$  passband. The uncertainties have been propagated. Plasma parameters:  $n_e(0)=1.13 \times 10^{19} \text{ m}^{-3}$ ,  $n_{Al}(0)=0.00108 \times 10^{19} \text{ m}^{-3}$ .

One final analysis was performed by analyzing the ratio of total signals from the  $T_{Zr}-T_{Si}$  and  $T_{Si}-T_{Al}$  passband [Figure 4.19]. The ratio is constant for  $T_e \geq 400 \text{ eV}$  but does vary at lower  $T_e$ . As a result, through using the two-color technique, NICKAL2 may have the ability to independently be used to determine  $T_e$  where this ratio varies strongly for  $T_e < 400 \text{ eV}$ . Similar to the analysis for  $n_e(0)$ , when using at least one passband, our measurement ranges have the lower bound of the lowest value  $T_{\min}$ . This is determined depending on which filter is used in the passband(s) for the measurement. When measuring the total Al line radiation and incorporating this into the SXT analysis, the lower bound is determined by  $T_{Zr}-T_{Al}$ , so  $T_{\min}^{(1)} \sim 225 \text{ eV}$ . For applying the two-color technique to the ratio of signals from two passbands or by partially

separating the charge states using the designated passbands,  $T_{\min}^{(2)} \sim 275 \text{ eV}$  as determined by  $T_{\text{Zr}}$ - $T_{\text{Si}}$  and  $T_{\text{Si}}$ - $T_{\text{Al}}$ .

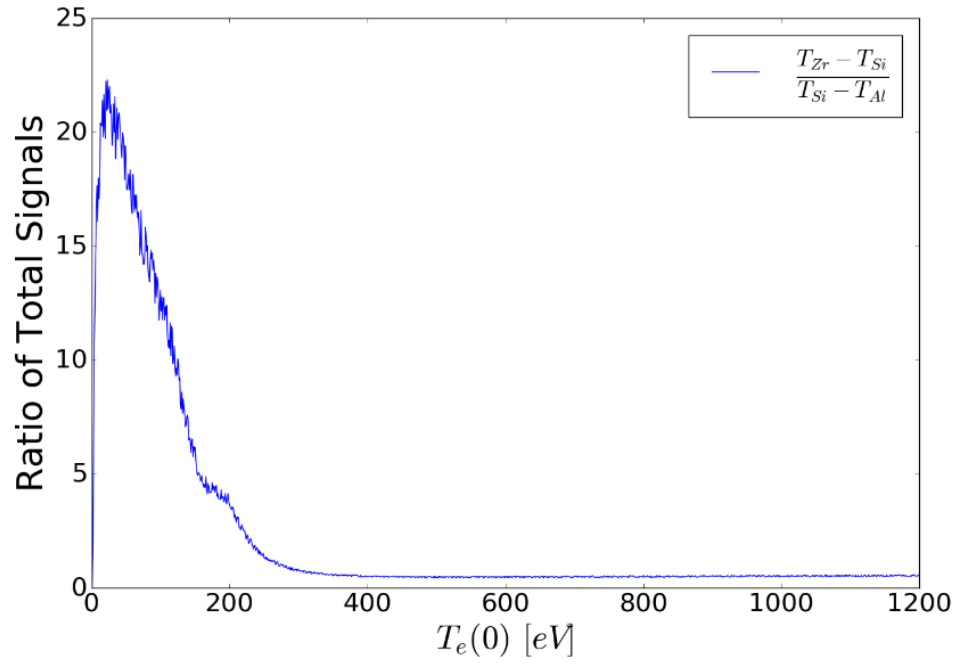


Figure 4.19: Simulated signal ratio of the total signal from the  $T_{\text{Zr}}\text{-}T_{\text{Si}}$  passband to the total signal from the  $T_{\text{Si}}\text{-}T_{\text{Al}}$  passband. The uncertainties have been propagated. Plasma parameters:  $n_e(0) = 1.13 \times 10^{19} \text{ m}^{-3}$ ,  $n_{\text{Al}}(0) = 0.00108 \times 10^{19} \text{ m}^{-3}$ .

## Chapter 5

### Conclusions and Future Work

A new diagnostic has been designed to effectively measure the Al<sup>11+</sup> and Al<sup>12+</sup> line radiation in MST. The major goal was to incorporate the total Al line radiation signal into the SXR analysis, allowing for thinner filters to be used in and lower T<sub>e</sub> explored when using the SXT system. This design was based off of previous work done on a Ross filter for measuring line radiation in the SXR spectrum of MST. In addition, the housing of the NICKAL2 detector was re-used from this previous work. It has three, angled lines of sight that eventually intersect. This housing posed no major constraints on designing the inner housing. In addition, the intersection of these lines of sight was found to be ~4.0 in. from the inner wall of MST, which, when combined with the ~8in. region of overlap, was acceptable for our measurement.

The inner housing utilizes three filtered AXUV-20G diodes. The final filter design was determined to be: 1.8μm Zr with 0.2μm Be, 6.8μm Al with 31.2μm Be, and 10.0μm Si with 12.7μm Be. This design allows for near optimal transmission of Al line radiation while absorbing most of the continuum emission. Through analysis of the transmission of each passband and signal via simulations, it was determined that the passbands all give different information.

The  $T_{Zr} - T_{Al}$  passband was found to be most effective in measuring the total Al line radiation. The  $T_{Zr} - T_{Al}$  passband can accurately measure the total Al line radiation at  $T_e \gtrsim 225$ . As a result, NICKAL2 has accomplished its major goal. Once measurements made by NICKAL2 are incorporated into the SXT system, it will likely extend the measurement range from  $T_e \geq 1$  keV to  $T_e \gtrsim 225$  eV. Secondly, the  $T_{Zr} - T_{Si}$  and  $T_{Si} - T_{Al}$  passbands were found to partially separate Al charge states. As a result,  $Al^{11+}$  line radiation can be more accurately measured for  $275 \leq T_e \leq 500$  eV. Through using other diagnostics and simulations, it may be possible to effectively determine the signal from each charge state within  $T_{Si} - T_{Al}$  passband. Finally, the two-color technique may be applied using only data from NICKAL2 to determine  $T_e$  for  $275 \leq T_e \leq 400$  eV.

As of now, all NICKAL2 components have been acquired and are being prepared for assembly. Once assembled, NICKAL2 will be tested on MST. This experimental data will be compared to simulation and checked for agreement. When the capabilities of the NICKAL2 detector have been experimentally proven, NICKAL2 will be incorporated into the Integrated Data Analysis tool and the SXT system, improving the  $T_e$  measurement range significantly.

## References

- [1] M. McGarry, “Probing the Relationship Between Magnetic and Temperature Structures with Soft X-Rays on the Madison Symmetric Torus,” Ph.D. thesis, University of Wisconsin – Madison, 2013
- [2] N. A. Pablant, R. E. Bell, M. Bitter, L. Delgado-Aparicio, K. W. Hill, S. Lazerson, and S. Morita, “Tomographic Inversion Techniques Incorporating Physical Constraints for Line Integrated Spectroscopy in Stellarators and Tokamaks,” Princeton Plasma Physics Laboratory, 2014
- [3] F. Bonomo et al., “2D characterization of core thermal topology changes in controlled RFX-mod QSH states,” Nucl. Fusion, 49, 4, 045011 (2009).
- [4] H.P. Summers. ADAS User Manual 2.6 [<http://www.adas.ac.uk/manual.php>], 2004.
- [5] B.L. Henke, E.M. Gullikson, and J.C. Davis. “X-ray interactions: photoabsorption, scattering, transmission, and reflection at E=50-30000 eV, Z=1-92”, Atomic Data and Nuclear Data Tables Vol. **54** (no.2), 181-342 (July 1993).
- [6] LEMO, “LEMO Website,” [<https://www.lemo.com/en>]
- [7] Opto Diode, “Opto Diode Website,” [<http://www.optodiode.com/>]
- [8] J. Waksman, “Neutral Beam Heating of a Reversed-Field Pinch in the Madison Symmetric Torus,” Ph.D. thesis, University of Wisconsin – Madison, 2013
- [9] J. W. Keister, "Silicon photodiodes for absolute soft x-ray radiometry," Proc. SPIE 6689, Solar Physics and Space Weather Instrumentation II, 66890U (20 September 2007)

- [10] Q. Xiao and G. Navratil, "A Photodiode for the Measurement of Soft X-ray Radiation from Plasma," *Rev. Sci. Instrum.*, vol. 67, no. 9, 1996
- [11] Ideal Vacuum Products, "Ideal Vacuum Products Website,"  
[<https://www.idealvac.com/Index.asp>]
- [12] N. Lanier, "Electron Density Fluctuations and Fluctuation-Induced Transport in the Reversed-Field Pinch," Ph.D. thesis, University of Wisconsin – Madison, 1999
- [13] P. A. Ross, *Phys. Rev.* 28, 425 (1926)
- [14] P. A. Ross, *J. Opt. Soc. Am.* and *Rev. Sci. Instrum.* 16, 433 (1928)
- [15] Tables of Physical & Chemical Constants (16<sup>th</sup> edition 1995). 4.2.1 X-ray absorption edges, characteristic X-ray lines, and fluorescence yields. Kaye & Laby Online. Version 1.0 (2005) [<http://www.kayelaby.npl.co.uk>]
- [16] Lebow Company, "Lebow Company Website," [<http://www.lebowcompany.com/>]